

A shear wave velocity model of the European upper mantle from automated inversion of seismic shear and surface waveforms

C. P. Legendre,^{1*} T. Meier,² S. Lebedev,³ W. Friederich¹ and L. Viereck-Götte⁴

¹*Institute for Geology, Mineralogy and Geophysics, Ruhr University Bochum, Bochum, Germany. E-mail: legendre@geophysik.ruhr-uni-bochum.de*

²*Geophysical Institute for Seismologie, Christian-Albrechts-Universität zu Kiel, Kiel, Germany*

³*Geophysics Section, Dublin Institute for Advanced Studies, Dublin, Ireland*

⁴*Institute of Mineralogy and Geochemistry, Friedrich-Schiller University Jena, Jena, Germany*

Accepted 2012 July 16. Received 2012 July 16; in original form 2012 January 2

SUMMARY

We present a new, *S*-velocity model of the European upper mantle, constrained by inversions of seismic waveforms from broad-band stations in Europe and surrounding regions. We collected seismograms for the years 1990–2007 from all permanent stations in Europe for which data were available. In addition, we incorporated data from temporary experiments. Automated multimode inversion of surface and *S*-wave forms was applied to extract structural information from the seismograms, in the form of linear equations with uncorrelated uncertainties. The equations were then solved for seismic velocity perturbations in the crust and mantle with respect to a 3-D reference model with a realistic crust.

We present two versions of the model: one for the entire European upper mantle and another, with the highest resolution, focused on the upper 200 km of the mantle beneath western and central Europe and the circum Mediterranean. The mantle lithosphere and asthenosphere are well resolved by both models. Major features of the lithosphere–asthenosphere system in Europe and the Mediterranean are identified. The highest velocities in the mantle lithosphere of the East European Craton (EEC) are found at about 150 km depth. There are no indications for a deep cratonic root below about 330 km depth. Lateral variations within the cratonic mantle lithosphere are resolved as well. The locations of kimberlites correlate with reduced *S*-wave velocities in the shallow cratonic mantle lithosphere. This anomaly is present in regions of both Proterozoic and Archean crust, pointing to an alteration of the mantle lithosphere after the formation of the craton. Strong lateral changes in *S*-wave velocity are found at the northwestern margin of the EEC and may indicate erosion of cratonic mantle lithosphere beneath the Scandes by hot asthenosphere. The mantle lithosphere beneath western Europe and between the Tornquist–Teisseyre Zone and the Elbe Line shows moderately high velocities and is of an intermediate character, between cratonic lithosphere and the thin lithosphere of central Europe. In central Europe, Caledonian and Variscian sutures are not associated with strong lateral changes in the lithosphere–asthenosphere system. Cenozoic anorogenic intraplate volcanism in central Europe and the circum Mediterranean is found in regions of shallow asthenosphere and close to changes in the depth of the lithosphere–asthenosphere boundary. Very low velocities at shallow upper-mantle depths are present from eastern Turkey towards the Dead Sea transform fault system and Sinai, beneath locations of recent volcanism. Low-velocity anomalies extending vertically from shallow upper mantle down to the transition zone are found beneath the Massif Central, Sinai and the Dead Sea, the Canary Islands and Iceland.

Key words: Tomography; Surface waves and free oscillations; Seismic tomography; Wave propagation; Cratons; Europe.

1 INTRODUCTION

Europe is characterized by a variety of tectonic provinces and structures, indicating complex tectonic processes active since the Precambrian (for summaries, see, e.g. Blundell *et al.* 1992; Cavazza

*Now at: Institute of Earth Sciences, Academia Sinica, Taipei, Taiwan.

et al. 2004; Gee & Stephenson 2006). In northeastern Europe, the cratonic region is of Precambrian age. It covers the East European Platform and the Baltic Shield. At the surface, the northwest–southeast trending Tornquist Zone marks the transition to Phanerozoic central Europe. South of the Tornquist Zone and north of the Rhetic Suture, Avalonian lithosphere is found. It was accreted to Laurussia during the Caledonian orogeny. Saxothuringian and American terranes and Gondwana collided with Laurussia in the north during the Variscian orogeny, resulting in the formation of the supercontinent Pangaea. The collapse of the Variscian orogen was followed by extensive magmatism and the development of up to 15-km-thick Mesozoic sedimentary basins adjacent to the southwestern margins of the East European Platform and the Baltic Shield. The break-up of Pangaea in the Jurassic was accompanied by the opening of mainly E–W trending oceanic basins in southern Europe and followed by the opening of the Atlantic Ocean and the formation of the Mid-Atlantic Ridge. The central and northern Atlantic Magmatic Provinces are indications of large-scale magmatic processes associated with the opening of the Atlantic Ocean. In addition, Atlantic hotspots beneath the Canary Islands, the Azores, Madeira and Iceland hint to the presence of still active hot upwellings with smaller lateral extent.

In the Mediterranean region, the tectonic development since the late Cretaceous is characterized by the convergence of Africa and Eurasia, by the closure of the Tethys Ocean and several smaller oceanic basins, and by the collision of Africa-derived terranes with Eurasia. In western and central Europe, Cenozoic intraplate volcanism occurred along a belt extending from the Massif Central to the Eifel region, the Vogelsberg, the Eger Rift and the Pannonian Basin.

The relation of these tectonic processes with upper-mantle structure has been a topic of a considerable number of tomographic investigations at different scales. The first studies are by Aki *et al.* (1977), Dziewonski *et al.* (1977), Woodhouse & Dziewonski (1984), Granet (1986) and Spakman (1988). In the following, we briefly summarize the main results that have been obtained by tomographic studies of the European upper mantle so far.

A 200–250-km-thick lithosphere in the cratonic region, indicated by high seismic velocities, has been imaged by surface wave studies on a global (Trampert & Woodhouse 1995; Grand *et al.* 1997; Masters *et al.* 2000; Grand 2002; Ritzwoller *et al.* 2002; Zhou *et al.* 2006; Peter *et al.* 2007; Lebedev & van der Hilst 2008; Boschi *et al.* 2009; Khan *et al.* 2011) as well as on a regional scale (Ritzwoller & Levshin 1998; Villaseñor *et al.* 2001b; Levshin *et al.* 2007; Weidle & Maupin 2008). The upper mantle beneath the neighbouring central Europe and northern Atlantic is characterized by low *S*-wave velocities from about 100 to 300 km depth, resulting in a strong lateral gradient across the margins of the cratonic mantle lithosphere (Zielhuis & Nolet 1994; Alsina & Snieder 1996; Marquering *et al.* 1996; Villaseñor *et al.* 2001a; Cotte *et al.* 2002; Deschamps *et al.* 2002; Schweitzer 2005; Dalton *et al.* 2009; Lin *et al.* 2009; Ritsema *et al.* 2011). These results have been confirmed by body wave studies in the adjacent region of the Tornquist–Teisseyre Zone (TTZ, Nolet & Zielhuis 1994; Plomerová *et al.* 2002; Shomali *et al.* 2006; Gregersen *et al.* 2010).

In the Aegean region, slab segments subducting into the lower mantle down to about 1400 km have been detected in global and regional studies (Spakman *et al.* 1993; Karason & van der Hilst 2000; Romanowicz 2003; Kassaras *et al.* 2005; Chang *et al.* 2010; van der Meer *et al.* 2010). In contrast, in the western Mediterranean and the Alpine region, the slab segments appear to be trapped within the mantle transition zone and do not dive deeper, according to body wave studies (Spakman *et al.* 1993; Piromallo & Morelli 1997;

Bijwaard & Spakman 2000; Wortel & Spakman 2000; Koulakov *et al.* 2002; Piromallo & Morelli 2003; Marone *et al.* 2004a,b; Schmid *et al.* 2008; Koulakov *et al.* 2009; Chang *et al.* 2010). Surface wave studies in the Mediterranean found low velocities below the lithosphere, especially in backarc regions (Endrun *et al.* 2004, 2008; Marone *et al.* 2004a,b; Fry *et al.* 2008; Boschi *et al.* 2009; Schivardi & Morelli 2009; Chang *et al.* 2010; Endrun *et al.* 2011; Ritsema *et al.* 2011). The presence of subducting slab segments in the European upper mantle has been confirmed by surface wave studies (Ritzwoller & Levshin 1998; Fry *et al.* 2008; Lebedev & van der Hilst 2008; Boschi *et al.* 2009).

In the Atlantic, inversions of body wave traveltimes show reduced seismic velocities consistent with deep reaching plumes beneath hotspots (Helmlinger *et al.* 1998; Bijwaard & Spakman 1999; Shen *et al.* 2002; Li & Detrick 2003; Montelli *et al.* 2006) although the detailed shape of plumes still remains to be imaged. Regional, tomographic studies indicate columnar low-velocity anomalies in the upper mantle beneath western and central European intraplate hotspots in the Massif Central (Granet *et al.* 1995) and the Eifel region (Ritter *et al.* 2001; Keyser *et al.* 2002) that seem to be confined to the upper mantle above the mantle transition zone (Ritter *et al.* 2001; Keyser *et al.* 2002; Plomerová *et al.* 2002; Pilidou *et al.* 2005). Beneath the Eger Rift, the presence of a small-scale upper-mantle plume has been ruled out (Plomerová *et al.* 2007; Babuška *et al.* 2010). Segments of subducting lithosphere in the upper mantle have been imaged in detail by local studies down to about 200 km depth beneath the Alps (Vaccari & Panza 1993; Fan *et al.* 1998; Lippitsch *et al.* 2003; Kissling *et al.* 2006; Raykova & Panza 2006; Panza *et al.* 2007), the eastern Carpathians (Kissling & Spakman 1996; Raykova & Panza 2006) and beneath the Pyrenees (Judenherr *et al.* 1999; Souriau *et al.* 2008).

Despite the large number of studies, the resolution of the European upper-mantle structure is still very heterogeneous, from tens of kilometres in the case of local studies to hundreds of kilometres in the case of global imaging, and generally decreases with depth. Furthermore, lateral and radial resolution of the models may vary strongly depending on the input data types. The lithosphere–asthenosphere system in the European upper mantle, the internal structure of the cratonic mantle lithosphere as well as details of the craton's boundaries with the Atlantic and central Europe still need to be resolved. The mantle transition zone in Europe remains particularly poorly resolved, with only a few, mostly large scale, features, such as the high *P*-wave velocity anomaly in the region of the Pannonian Basin, imaged by several studies (Spakman *et al.* 1993; Kissling & Spakman 1996; Wortel & Spakman 2000; Piromallo *et al.* 2001; Piromallo & Morelli 2003; Dando *et al.* 2011). In addition, the shape and the internal structure of the slab segments in the upper mantle are still a matter of debate.

Increased resolution of the upper-mantle structure can be achieved by extracting more information from broad-band seismic waveforms, by processing all available broad-band data and by improving upon approximations of wave propagation that form the basis of the tomographic inversion. Inversion of waveforms was first based on normal mode theory (Woodhouse 1974) and later extended to broader frequency bands, up to about 50 mHz, using surface wave mode summation (Nolet *et al.* 1994; Marquering *et al.* 1996). A fully automated processing scheme (automated multimode inversion, AMI) was proposed by Lebedev *et al.* (2005). An improved model parametrization on a spherical grid, inversion for crustal structure relative to a 3-D reference model, as well as waveform fitting in automatically selected portions of the time–frequency plane were introduced to improve the robustness and accuracy of

the inversion and to process large data sets. Parts of the waveform that may be explained by the Jeffreys–Wentzel–Kramers–Brillouin (JWKB, Dahlen & Tromp 1998) approximation are identified and inverted using sensitivity kernels that approximate the first Fresnel volume. Applications to benchmark data sets showed that AMI provides accurate, high-resolution images of upper-mantle structure down to the transition zone (Lebedev & van der Hilst 2008; Qin *et al.* 2008). To explain more complicated waveforms, caused by strong lateral heterogeneity and not utilized by AMI, wave-propagation complexity and finite frequency effects have to be modelled and accounted for (Friederich *et al.* 1993; Wielandt 1993; Friederich *et al.* 1994; Trampert & Woodhouse 1995; Trampert & Woodhouse 1996; Meier *et al.* 1997b; Levshin *et al.* 2005; Peter *et al.* 2007; Fichtner *et al.* 2008; Bozdağ *et al.* 2011; Fichtner & Trampert 2011).

We present a new high-resolution, *S*-wave velocity model of the upper mantle below Europe, including the transition zone, resulting from waveform inversion of all available data from European broadband stations, by means of AMI (Lebedev *et al.* 2005). The inversion is global, to account for heterogeneity outside the region of interest.

The presented model may serve as a European reference shear wave velocity model, because, first, all available data between 1990 and 2007 have been inverted for *S*-wave velocity distribution in the entire upper mantle beneath Europe. Secondly, the model shows the maximum resolution currently achievable with the JWKB approximation, used for the inversion of long-period waveforms. Thus, it can serve as a background model for tomographic inversions accounting more precisely for finite frequency effects. In the following, we describe the derivation of the model, identify its main features and discuss the relations of mantle *S*-velocity structure to surface tectonics and volcanism.

2 METHOD

2.1 Automated multimode inversion (AMI)

We apply the AMI method, described in detail by Lebedev *et al.* (2005) and Lebedev & van der Hilst (2008), to determine a shear wave velocity model of Europe and surrounding regions, from the crust down to the transition zone. AMI is a three-step inversion procedure, based on the partitioned waveform inversion scheme (Nolet 1990) and designed to handle very large amounts of data automatically. In its first step, AMI derives linear constraints on 3-D, *S*- and *P*-velocity structure by performing non-linear waveform fitting on individual seismograms, each constraining structure along one source–receiver path.

The basic requirement for the first step is that each recorded seismogram can be well modelled by a synthetic seismogram, computed with a path-average modal superposition approach. Because this requirement may be met depending on the considered frequency band and time window, the data and synthetics are passed through a series of Gaussian bandpass filters and the misfit is evaluated in multiple time windows, which may include the fundamental-mode surface waves and the *S*- and multiple *S*-body waves. Any combination of the time window and frequency band for which the misfit exceeds a pre-defined level (5 per cent) is eliminated from the data set. To avoid chance fits, accepted fundamental-mode time windows must come from an uninterrupted series of Gaussian filters with increasing centre frequency. In addition, we discard time–frequency windows with too low signal-to-noise ratio or windows recorded at near-nodal azimuths of the radiation pattern since they may

contain significant scattered energy, not modelled by the path-average modal superposition approach.

The non-linear waveform inversion of the signal in the accepted time–frequency windows provides an estimate of the average perturbation of shear wave velocity within the approximate sensitivity volume between the source and receiver, as a function of depth. It is parametrized using a linear combination of basis functions whose expansion coefficients are the ultimate result of the first inversion step. The coefficients provide linear constraints on the 3-D velocity perturbations which can be expressed as integrals over kernels, determined primarily by the chosen basis functions. Once a discrete parametrization for the 3-D velocity distribution is chosen, these integrals can be converted to linear equations with uncorrelated uncertainties. Fig. 1 shows examples of bandpassed waveforms and their synthetic counterparts for two different events before and after non-linear inversion. The bottom panels show the estimated, path-average *S*-wave velocity models constructed from the expansion coefficients determined in the inversion.

In the second step, the constraints from all available time–frequency windows from different source–receiver paths, formulated as linear equations, are collected into one large system of equations which is solved, subject to regularization, for 3-D, *S*- and *P*-velocity perturbations using LSQR (Paige & Saunders 1982). Radially, the 3-D model is parametrized, same as the waveform inversions, using 18 parameters for *S* velocity and 10 parameters for *P* velocity. To avoid trade-offs between *P*- and *S*-velocity perturbations, which cannot be resolved by shear and surface waveforms, we regularize the inversion by introducing an elastic coupling between the two which may be violated if required by the data.

A common solution for this is to introduce a rigid coupling between *P*- and *S*-velocity heterogeneity. In our tomographic inversion, perturbations in *P* velocities are strongly damped towards being the same as those in *S* velocities ($dV_p \text{ (m s}^{-1}\text{)} = dV_s \text{ (m s}^{-1}\text{)}$): we penalize the difference between dV_p and dV_s . We thus introduce a coupling between dV_p and dV_s but allow deviations from it, in case the data require them in some locations (Lebedev & van der Hilst 2008).

The third step performs an *a posteriori* cleaning of the data set by removing outliers. Given the 3-D perturbations of velocity, expansion coefficients of the path-specific average velocity perturbations are calculated and compared to the expansion coefficients obtained from non-linear waveform inversion. Source–receiver paths with excessive deviations are eliminated from the data set and the 3-D inversion is repeated.

2.2 3-D reference model

Successful waveform inversion partly depends on an appropriate choice of an initial model (Dziewonski & Anderson 1981; Kennett *et al.* 1995; Rawlinson *et al.* 2010). The non-linear waveform inversions yield 1-D path-average perturbations with respect to a global 3-D reference model. This initial reference model is composed of a 3-D global crustal model (CRUST2.0, Bassin *et al.* 2000, smoothed near cell boundaries) and the 1-D standard earth model AK135 (Kennett *et al.* 1995) reevaluated at a reference period of 50 s (Lebedev *et al.* 2005). The linear equations obtained from processing of all the seismograms are inverted for seismic velocity perturbations relative to the same reference model. Therefore, we invert also for the crustal structure in addition to upper-mantle structure. CRUST2.0 is used only to calculate initial synthetics that are subsequently fitted to the data. This implies CRUST2.0 serves as

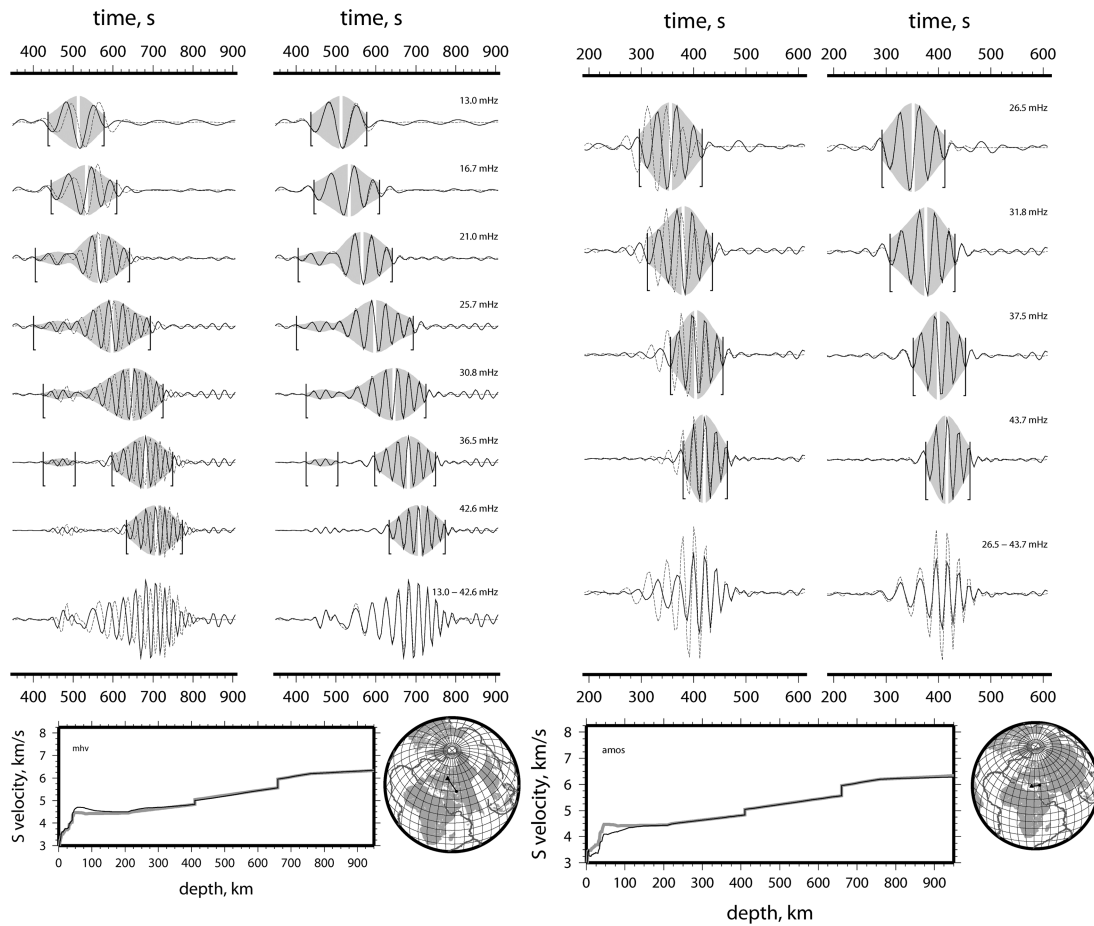


Figure 1. Top panels: Comparison of filtered data (solid) and synthetic seismograms (dashed) before and after non-linear waveform inversion for two different paths. In the upper panels, the left column shows data and synthetics before inversion, the right column after inversion. Different rows in each panel show seismograms bandpassed filtered in ascending frequency ranges. The bottommost row displays the assembled observed and synthetic seismograms. Bottom panels: Initial (grey) and perturbed (black) path-specific *S*-velocity models and a map displaying the associated great circle path.

a 3-D background model but is not used for crustal corrections. The perturbations at depths shallower than 50 km to this background model are large; uncertainties in the reference crustal model are unlikely to cause substantial errors in the 3-D model at depths larger than 50 km.

2.3 Parametrization and regularization

The 3-D perturbations of seismic velocities are determined at the knots of a global triangular grid covering the Earth’s surface with an approximately equal, 100 km interknot spacing. Radially, the parametrization is organized as concentric shells with the same knot coordinates. To perform the integration that relates the expansion coefficients of the path-specific, average velocity models to 3-D perturbations, we use a denser triangular grid, with knot spacing about a sixth of that of the model grid (Fig. 2).

The 3-D inversion is regularized by horizontal and vertical smoothing as well as slight norm damping. Although we show only isotropic perturbations of *S*-wave velocity, we allow azimuthal *S*-velocity variations during the inversion, to avoid mapping anisotropy into the isotropic heterogeneities. The lateral smoothing penalizes the difference between the anomaly at a knot and the average over the anomalies at this and the six neighbouring knots.

A minor contribution of norm damping component is thus also integrated in the smoothing term. The strength of the lateral smoothing may vary with depth, to allow a flexible response to variations of path coverage with depth. (This is discussed further in Section 4.) Path coverage is estimated from the sums over columns of the matrix of the equation system which represent the relative importance of a knot in the inversion. Vertical smoothing penalizes the difference of the anomaly at a knot and the average of its immediate neighbours above and below. Because in most practical cases the path coverage is irregular, we also identify similar paths and downweight each of them during the inversion by a factor proportional to the number of paths similar to it. The similarity of the paths depends on the locations of the sources and receivers.

3 DATA

3.1 Seismic stations

For this study, a dedicated effort was made to gather a fairly complete collection of data from broad-band stations located in Europe. The vertical component seismograms with a length of up to 4000 s of the BH (20 Hz) and LH (1 Hz) channels were downloaded from the data centres of Incorporated Research Institutions for

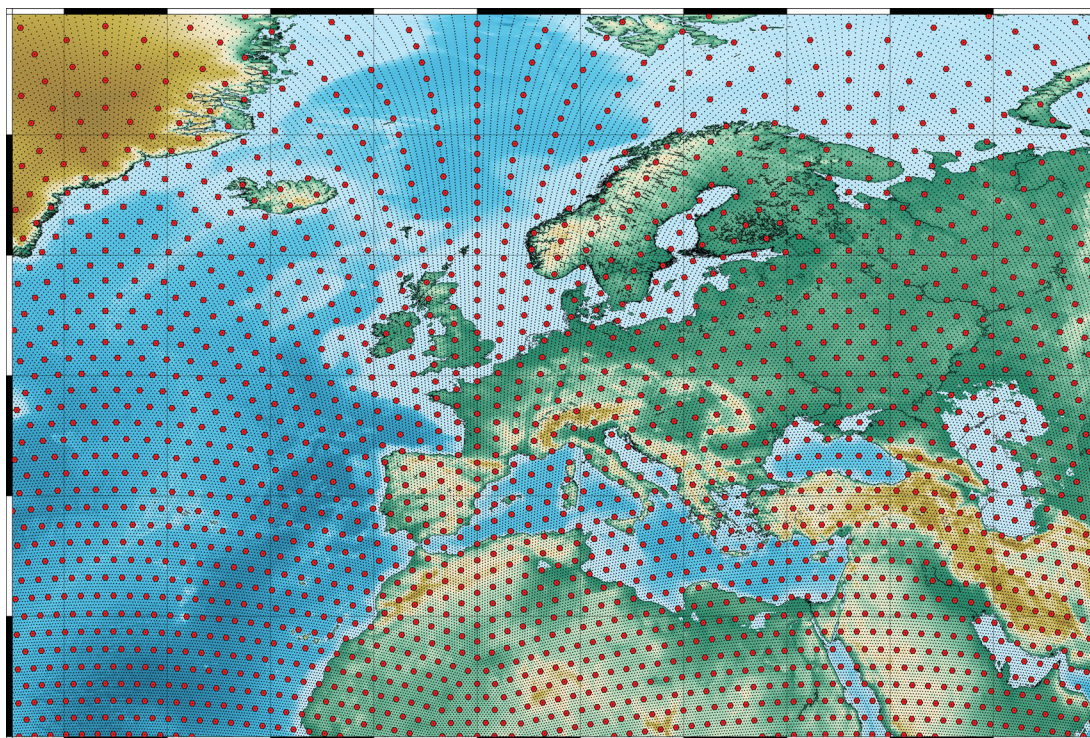


Figure 2. Location of knots (red dots) used for parametrization of S - and P -velocity perturbations. The integral relating path-average perturbations to 3-D perturbations is performed over the grid represented by the small dots.

Seismology (IRIS), GEOFON and Observatories and Research Facilities for European Seismology (ORFEUS), as well as from the Réseau National de Surveillance Sismique (ReNaSs). A complete list of the networks which provided data that entered this study is given in Table 1. In addition to permanently operating seismic stations, we incorporated data from national networks and also from temporary deployments, such as TOR (teleseismic tomography experiment across the TORnquist Zone, Arlitt *et al.* 1999; Cotte *et al.* 2002), SVEKALAPKO (SVEcofennian–KARElia–LAPland–KOLA, Bock *et al.* 2001), EP (Eifel Plume, Ritter *et al.* 2001; Keyser *et al.* 2002) and EGELADOS (Exploring the GEodynamics of subducting Lithosphere using an Amphibian Deployment Of Seismographs, Friederich & Meier 2008). For additional coverage beyond Europe, we also included some stations of the GSN (global seismograph network) located in North America, Asia and Africa. Locations of all the stations are shown in Fig. 3. This represents a total of 1033 broad-band stations, as summarized in Table 1.

3.2 Earthquake selection

Since the focus of the study is Europe and surroundings, we collected records of all earthquakes occurring in and around Europe between 1990 and 2007, down to a magnitude of 3.5. These data were supplemented by records of worldwide earthquakes with distances up to 15 000 km from Europe and with moment magnitudes down to 4.5. A map of the epicentres is shown in Fig. 4. In total, 11 000 events were recorded on about 700 000 seismograms were collected. The actual number of seismograms entering the inversion is smaller than that, because many data, in particular from small events at larger distances, display signal-to-noise ratios that are too low.

3.3 Quality checks and rejection criteria

The collected seismograms are subjected to rigorous quality checks. To begin with, we collected data only from earthquakes with a magnitude above a distance-dependent magnitude threshold. Then, each seismogram was checked for signal-to-noise-ratio (all seismograms with a signal-to-noise ratio lower than five are discarded), occurrences of multiple events as well as clipped or missing data. Observed and predicted arrival times for body and surface waves are compared to reject traces from earthquakes with large origin time errors or traces from stations with timing errors.

Because the method requires the validity of the JWKB approximation (Dahlen & Tromp 1998), we verify for each seismogram whether it can be well modelled by a synthetic seismogram computed with a path-average modal superposition approach. To this end, data and synthetics are passed through a series of Gaussian bandpass filters with frequency-dependent widths and the misfit is evaluated in multiple time windows, which may include S - and multiple S -body waves and the fundamental-mode surface waves. The misfit thresholds in this step is highly conservative (5 per cent) and an acceptable fit must be obtained for three or more consecutive frequency bands (Fig. 1).

At this stage, 78 000 seismograms remain, which provide about 320 000 linear constraints on the model. Finally, after inversion for a 3-D S -velocity model, we perform an additional *a posteriori* cleaning of the data set from outliers. The data predicted by the 3-D model are compared to the observed ones and residuals are calculated (Fig. 5). Equations associated with large residuals are eliminated from the linear system of equations and the inversion is repeated. Our experience shows that artefacts in the 3-D-model caused by errors in the data can be removed effectively by this procedure.

Table 1. Network code for the stations used for this study. LHZ refers to a sampling rate of 1 Hz, whereas BHZ refers to a sampling rate of 20 Hz and HHZ corresponds to 100 Hz. The data centres are: I (IRIS), G (Geoscope), Ge (GEOFON), O (ORFEUS).

Network code	Amount of stations	Channel available	Network name	Data centre
AF	29	(BHZ)	Africa Array	I, Ge
BE	3	(HHZ)	Belgian Seismic Network	O
BN	5	(LHZ)	UK-Net	O
BS	2	(BHZ)	National Network of Bulgaria	O
BW	3	(BHZ)	BayernNetz (Germany)	O
CA	3	(LHZ)	Catalan Seismic Network (Spain)	O
CD	8	(LHZ)	China Digital Seismograph Network	I
CH	27	(BHZ)	Switzerland Seismological Network	O
CN	1	(LHZ)	Canadian National Seismograph Network	I
CR	1	(BHZ)	Croatian Seismograph Network	O
CZ	9	(LHZ)	Czech Regional Seismic Network	I, Ge
DK	3	(BHZ)	Danish Seismological Network	Ge
EN	163	(LHZ)	EGELADOS Network, deployed in Greece and Turkey	Ge
EP	26	(LHZ)	EIFEL PLUME Network	Ge
ES	4	(BHZ + HHZ)	Spanish Digital Seismic Network	O
FN	1	(BHZ)	Sodankyl Geophysical Observatory (Finland)	Ge, O
FR	18	(LHZ + BHZ)	French Broadband Seismological Network	O
G	12	(LHZ + BHZ)	GEOSCOPE (France)	I, G, Ge, O
GB	12	(BHZ)	Great Britain Seismograph Network	O
GE	54	(LHZ + BHZ)	GEOFON (Germany)	I, Ge, O
GR	27	(LHZ + BHZ)	German Regional Seismic Network	Ge, O
GT	4	(LHZ)	Global Telemetered Seismograph Network (USAF/USGS)	I
HE	6	(BHZ)	Finnish National Seismic Network	Ge, O
HF	1	(BHZ)	Swedish Seismic Array Network	O
HL	4	(BHZ)	National Observatory of Athens Digital Broadband Network	Ge, O
HP	1	(BHZ)	University of Patras (Greece)	O
HT	16	(LHZ + BHZ)	Aristotle University Thessaloniki Network	Ge
HU	3	(BHZ)	Hungarian Seismological Network	Ge, O
IC	10	(LHZ)	New China Digital Seismograph Network	I
II	26	(LHZ + BHZ)	Global Seismograph Network (GSN—IRIS/IDA)	I, O
IP	2	(BHZ)	Instituto Superior Tecnico Broadband Seismic (Portugal)	O
IU	31	(LHZ + BHZ)	Global Seismograph Network (GSN—IRIS/USGS)	I, O
KN	12	(LHZ)	Kyrgyz Seismic Telemetry Network (Kyrgyzstan)	I
KO	7	(BHZ)	Kandilli Observatory (Turkey)	Ge, O
MN	26	(LHZ + BHZ)	MEDNET	I, Ge, O
MS	1	(LHZ)	IRIS/Singapore, Singapore National Network (GSN)	I
NL	4	(LHZ + BHZ)	Netherlands Seismic Network	O
NO	3	(LHZ + BHZ)	Norwegian Seismic Array Network	O
NR	1	(BHZ)	NARS Array	O
OE	13	(BHZ)	Austrian Seismic Network	Ge, O
PL	4	(LHZ + BHZ)	Polish Seismological Network	Ge, O
PM	2	(BHZ)	Portuguese National Seismograph Network	Ge, O
PS	2	(LHZ)	Pacific21	I
RO	7	(BHZ)	Romanian Seismic Network	Ge, O
SK	3	(BHZ)	Slovak National Seismic Network	Ge, O
SL	10	(LHZ + BHZ)	Slovenia Seismic Network	O
SS	1	(BHZ)	SINGLE STATION (Spain)	O
SV	62	(LHZ)	SVEKALAPKO Network (Finland)	Ge
TO	55	(LHZ)	TOR Network (deployed in Germany, Denmark and Sweden)	Ge
VI	1	(BHZ)	SIL-Icelandic National Digital Seismograph Network	O
YL	29	(LHZ)	North Anatolian Fault	I

Fig. 5 demonstrates that the residuals between the observed and calculated constraints are limited. This can be explained by the highly rigorous selection of the data set. The residuals calculated for a smooth model or a rough model (*cf.* Section 5) are quite similar. Most of the data set is confined to very low residuals, and less than 1 per cent of the data exhibit large deviations from the calculated model. The differences between the deviations from the rough and the smooth models are small, and mostly lie in the high-deviation part of the distribution. The *a posteriori* cleaning of the data set

from outliers is performed by removing 1 per cent of the data that exhibit the largest deviations from the calculated model.

3.4 Statistical properties of the data set

During the initial waveform fitting step, time windows are identified for which an acceptable fit of the bandpassed seismogram can be obtained. Fig. 6 shows a compilation of all accepted time windows in a time–distance plot, with ‘arrival times’ estimated to be at maxima

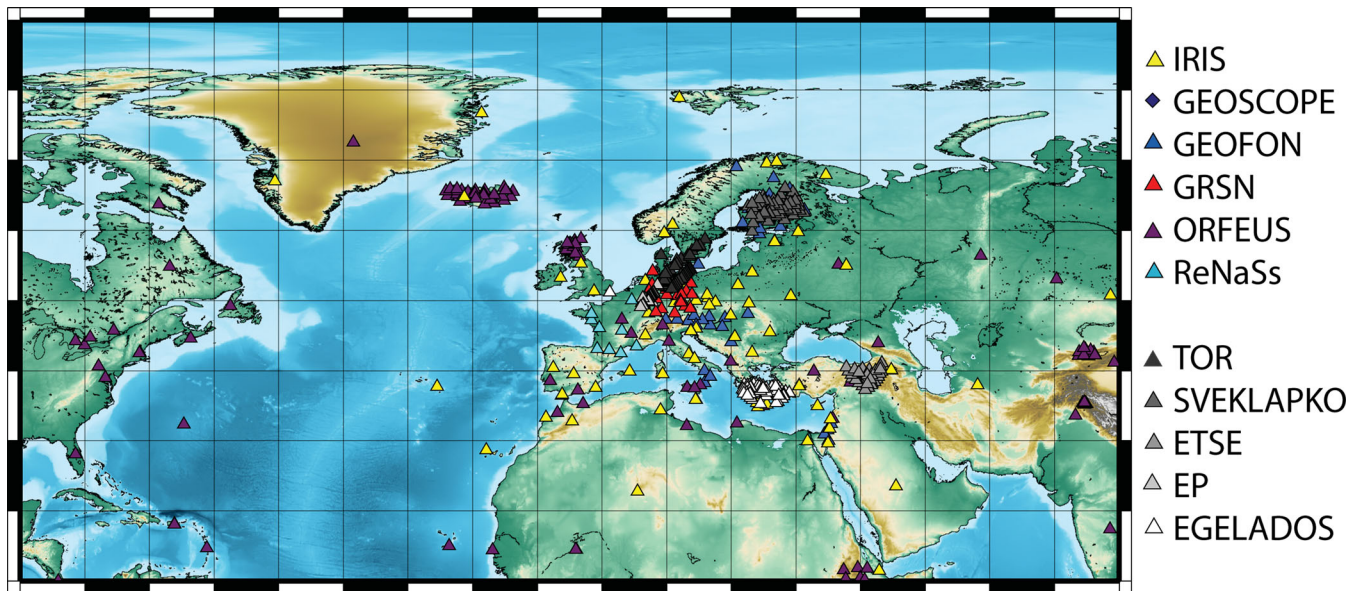


Figure 3. Map of the broad-band stations used for the study. Permanent stations are shown in colours whereas temporary deployments are shown in shades of grey.

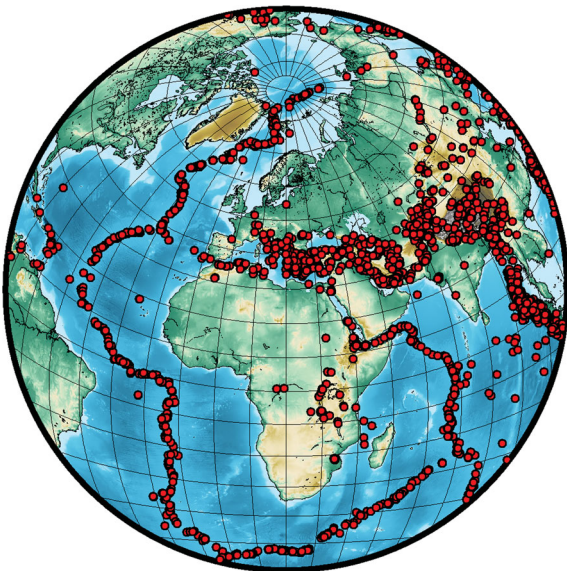


Figure 4. Geographical distribution of earthquakes used in this study. Epicentres are indicated by red dots.

of the signal envelope within all selected time windows. Most of the time windows contain the fundamental-mode, Rayleigh-wave train. *S*-wave arrivals split into direct *S* phases at short distances and multiple *S* phases at longer distances.

Fig. 7 displays the number of accepted seismograms as a function of epicentral distance. The bimodal form of the distribution is caused by the event and station selection strategy which focused on paths covering Europe supplemented by teleseismic data that provide constraints on the surrounding regions.

Constraints on the 3-D model are derived from a simultaneous fit of the signal in the accepted time–frequency windows, and the frequency range of the windows is generally different for each seismogram. The information content of the windows that contain the fundamental mode varies with frequency. This is visualized in Fig. 8, left-hand panel, where we show the distribution of accepted

fundamental mode wave trains versus frequency. There is a clear maximum at about 10 mHz with a gradual fall-off towards high frequencies. As the sensitivity of the fundamental-mode surface waves is confined within the upper 300 km for frequencies down to 10 mHz (see Fig. 8, right-hand panel), we expect the best resolution of the data set in this depth range. Sensitivity for greater depths comes mainly from the *S*-wave trains at intermediate-to-large epicentral distances, as well as from very long period fundamental-mode wave trains. The main effect of the cross-branch coupling in this context is that *S* and multiple *S* waves have sensitivity volumes that are substantially different from the simple path averages assumed in our inversions. The effect of this can be very large in inversions of small data sets but is reduced when the path coverage is very dense, as in this study, and especially when both *S* and multiple *S* waves are included (their combined sensitivity volumes filling the volumes between sources and stations so that the validity of the path-average approximation increases). As confirmed by ground-truth tests such as the location of subducted slabs (known from seismicity) and by spectral-element tests (Lebedev & van der Hilst 2008; Qin *et al.* 2008), the locations of deep anomalies can be retrieved accurately with the approximations assumed, although the amplitudes of all transition-zone anomalies are underestimated.

The spatial distribution of sensitivity of the data set to variations of seismic velocities at depth is controlled laterally by a combination of the path coverage, the available frequency range and the available seismic phases. A convenient measure for this sensitivity is the column sum of the matrix of linear constraints which collects the sensitivity of all available data with respect to a single-velocity grid knot of the 3-D model. Therefore, according to the frequency content and the sensitivity kernels, it is possible to calculate the density of information provided by the data for each point at each depth. Fig. 9 shows horizontal cross-sections of this collective sensitivity measure, highest in central and southeastern Europe and the Middle East and thus dominated by the distribution of stations and seismic events. Most of the stations are located in Europe, and the earthquakes mostly occur in the convergence zone of Africa, Arabia and India with Eurasia. At shallow depths, the influence of the surface waves is dominant. At greater depths, however, the influence

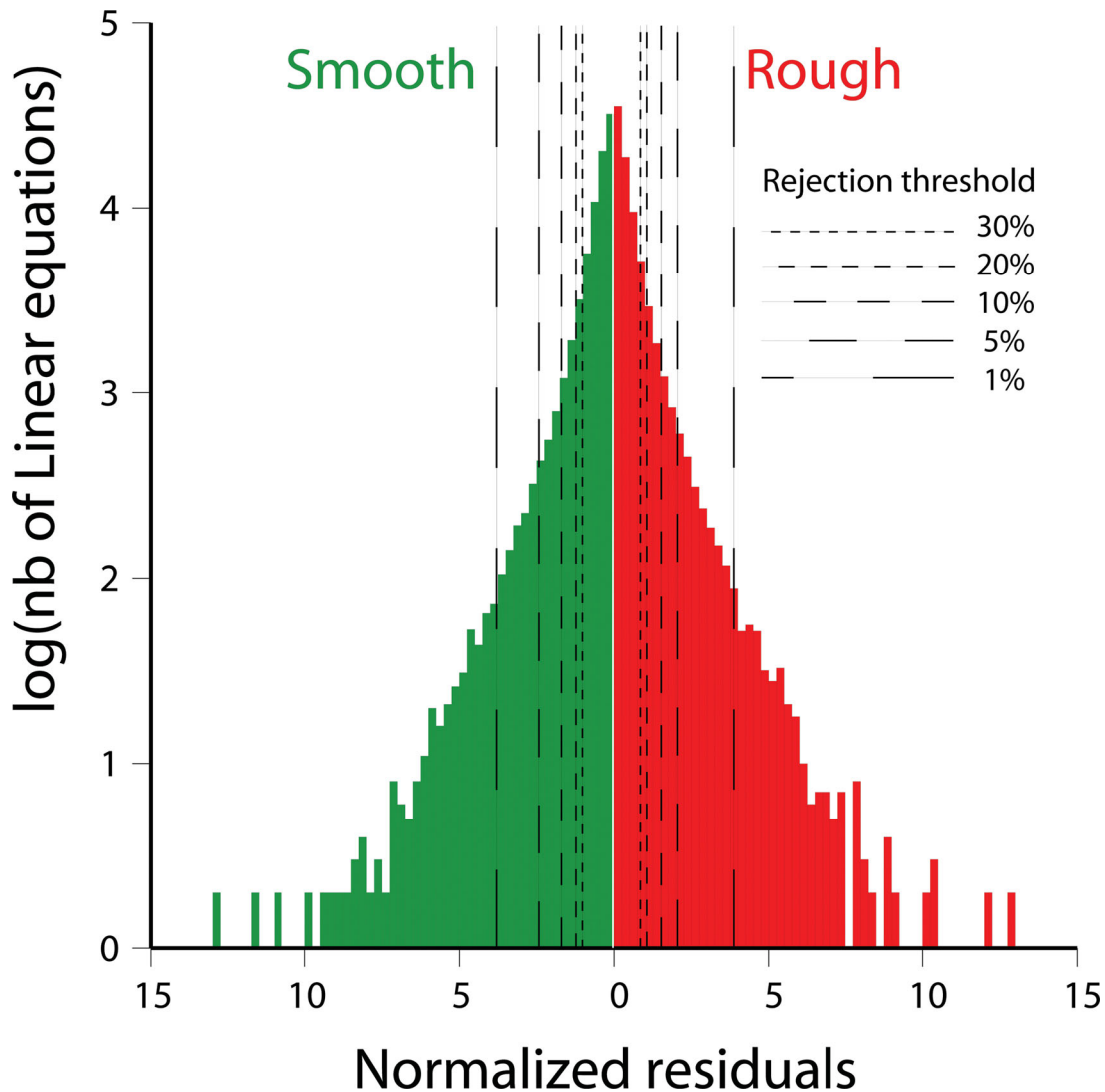


Figure 5. Histograms showing the number of linear equations versus their associated *a posteriori* residuals. The left part of the figure presents the residuals calculated for a smooth version of the model whereas the right part of the figure illustrates the residuals for a rougher model. The dashed lines illustrate the residual threshold necessary to reject, respectively, 1, 5, 10, 20 and 30 per cent of the data set.

of the S and multiple S waves is more important. In central Europe, the amount of information for each knot is the highest, implying higher resolution in this area (subject to the forward modelling and the sensitivity kernels being sufficiently accurate).

4 RESOLUTION TESTS

Resolution is mainly controlled by the cumulated sensitivity of the available data to velocity perturbations of the medium but also by additional *a priori* constraints such as norm damping and smoothing. Here, we discuss the influence of the latter two on the properties of the resulting model.

Lateral smoothing penalizes the difference between the anomaly at a knot and the average of the anomalies at the six neighbouring knots. Vertical smoothing penalizes the difference between the anomaly at a knot and the averaged anomalies of the two knots above and below. The lateral smoothing weights vary with depth. Since cumulated data sensitivity of our data set decreases with depth, we choose lateral smoothing weights such that the effective smoothing

increases with depth. Fig. 10 demonstrates the effect of smoothing on the resulting velocity model at 80 km depth for a grid spacing of 100 km and constant norm damping.

If the smoothing weight is too low, small-scale artefacts may appear in the regions with lower data sensitivity, such as in the Atlantic Ocean in Fig. 10 (upper left panel). If the smoothing weight is, instead, too high, we may lose information on small-scale features (Fig. 10, bottom right). Therefore, we aimed to select a smoothing weight large enough to avoid artefacts but such that it still permitted to resolve small-scale anomalies.

In many tomographic studies, checkerboard tests are employed to assess resolution. Here, we follow a different approach, as in Bijwaard *et al.* (1998) and Qin *et al.* (2008). As a test model, we use a constant high-velocity anomaly in combination with small spiked low-velocity anomalies. Then we computed synthetic linear constraints from this test model and performed an inversion to recalculate the model from the synthetic linear constraints, with the actual path coverage. This allows testing for both the reconstruction of the background, which should not be distorted or attenuated, and spike anomalies, where the amplitudes, width and location of which

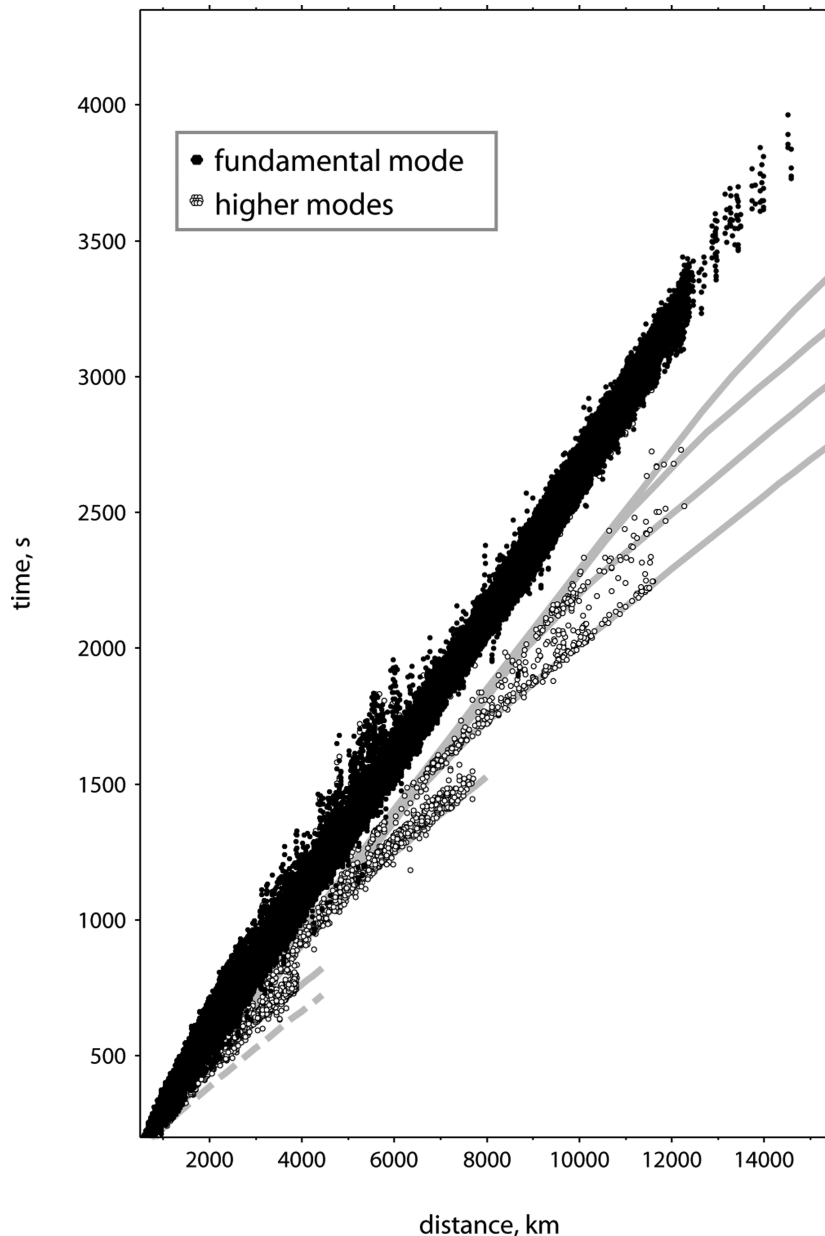


Figure 6. Distribution of the time windows that provided constraints for the inversion (i.e. the windows within which the waveforms were fit successfully), with respect to seismic wave arrival time, distance and wave type. Dots mark the epicentral distance and the centre of the time window for the fundamental-mode (black) or the higher mode (light grey) wave trains. Solid grey curves show the predicted arrival times of the S - and multiple S waves from a surface source; the dashed grey line shows the predicted arrival time of the S waves from a 660-km-deep source.

should be correctly retrieved. The equally spaced spikes are used to test for possible smearing or mislocation of anomalies in the model. The velocity perturbations are $\delta V_s = +100 \text{ m s}^{-1}$ for the constant background and $\delta V_s = -100 \text{ m s}^{-1}$ for the spikes. The anomalies are placed at one depth, and we invert for all depth, to check the vertical smearing.

In a first step, we make use of a resolution test to determine appropriate weights for norm damping which is used to constrain the amplitude of the velocity perturbations. Norm damping is described by two numbers: the damping weight at the surface and its vertical gradient. The effect of both parameters has been investigated by inverting synthetic test models, to calibrate our inversion.

Norm damping has negligible effects on the lateral distribution of the resulting anomalies. Moreover, the resolution tests allow us to

adjust the damping parameter in such a way that the input anomalies are properly retrieved after inversion.

With the damping and smoothing constraints adjusted as described earlier, resolution tests for models with a grid spacing of 100 km and two different smoothing weights (hereinafter referred to model I for the smooth version and model II for the roughest version) have been performed. Figs 11 and 12 show results of resolution tests for models I and II, respectively. All tests demonstrate a satisfactory recovery of both the spikes and the background. Fig. 11 shows that for the uppermost mantle (80–200 km depth), the background is accurately recovered without distortion over the entire region investigated. At these depths, most of the spikes are properly reconstructed, both in amplitude and in location. No lateral smearing or mislocation is observed. A few spikes are not fully retrieved,

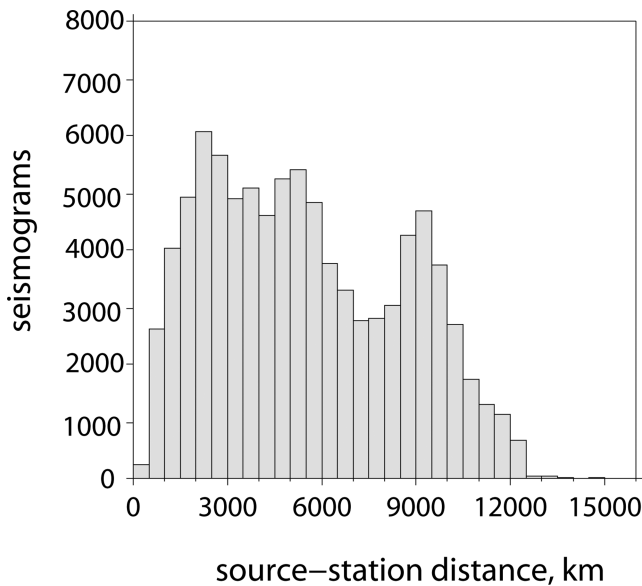


Figure 7. Histogram showing the distribution of the seismograms versus epicentral distance.

a fact which seems to be directly related to spatial variations of sensitivity (Fig. 9), with low values in the Atlantic region or in the easternmost part of Europe. Resolution declines with depth as demonstrated by resolution tests at 410 and 585 km depth shown in the bottom panel of Fig. 11. Only the spikes in central Europe are properly recovered.

At 410 km depth, the spikes are smeared in regions with sparser coverage and only 50–60 per cent of the anomaly amplitude is recovered for most of the spikes. At 585 km depth, in the Atlantic region or in the easternmost part of Europe, the spikes are smeared out.

Tests with less smoothing (model II) demonstrate that the data set allows the retrieval of more detailed structure, especially in central Europe where the path coverage is highest (Fig. 12). The smearing of the spikes is weaker than for the model I, and the background is accurately recovered (no distortion or variation in amplitude) for the upper 200 km, where the path density (Fig. 9) is the highest. We refrain from showing resolution tests for greater depths because we will not interpret model II there and because we do not expect any improvement of resolution over model I at these depths.

The resolution tests presented here targeted the coverage given by the data and did not include errors in the data. The main sources of

errors are the locations and origin times of the events and diffraction effects not accounted for by the approximate sensitivity kernels that we used. Given the very substantial redundancy of our coverage, provided by the tens of thousands of seismograms, random errors are unlikely to have any significant impact on the results. Systematic errors are of more concern, but guessing what they are, to design a relevant test, is not straightforward.

Lebedev *et al.* (1997) performed partitioned waveform inversion on a (much smaller) data set from the Philippine Sea region using, first, earthquake locations and origin times computed using short-period body wave arrivals (NEIC – National Earthquake Information Center Centroid Moment Tensor) and, alternatively, using Harvard CMT source parameters. Despite substantial systematic differences between the source parameters in the two catalogues, anomalies in the resulting regional tomographic models did not differ substantially. The possible effects of diffraction were tested in numerical (spectral element method, SEM) resolution tests using AMI (Lebedev & van der Hilst 2008; Qin *et al.* 2008) and did not prevent an accurate recovery of anomalies that were sufficiently well sampled by crossing rays. These previous tests suggest that the effect of errors in the data is limited if the data sampling is sufficiently dense, which is what we have tested here.

5 DISCUSSION OF THE 3-D UPPER-MANTLE *S*-WAVE MODELS

In this section, we would like to discuss the main and well-resolved features of models I and II. In addition, their relation to tectonic processes is discussed qualitatively. The models I (Fig. 13) and II (Fig. 14) can be used in further, more quantitative investigations in the future.

5.1 The East European Craton (EEC)

High *S*-wave velocities down to 200 km depth (perturbations up to 4–8 per cent) are found in the region of the EEC. These were detected already by early global tomography (e.g. Woodhouse & Dziewonski 1984; Zhang & Tanimoto 1993). These findings were confirmed repeatedly by later, large-scale surface wave studies (Masters *et al.* 2000; Mégnin & Romanowicz 2000; Ritzwoller *et al.* 2002; Ritsema *et al.* 2004; Levshin *et al.* 2005; Pilidou *et al.* 2005; Shapiro *et al.* 2005; Panning & Romanowicz 2006; Priestley & McKenzie 2006; Zhou *et al.* 2006; Peter *et al.* 2007; Lebedev & van der Hilst 2008;

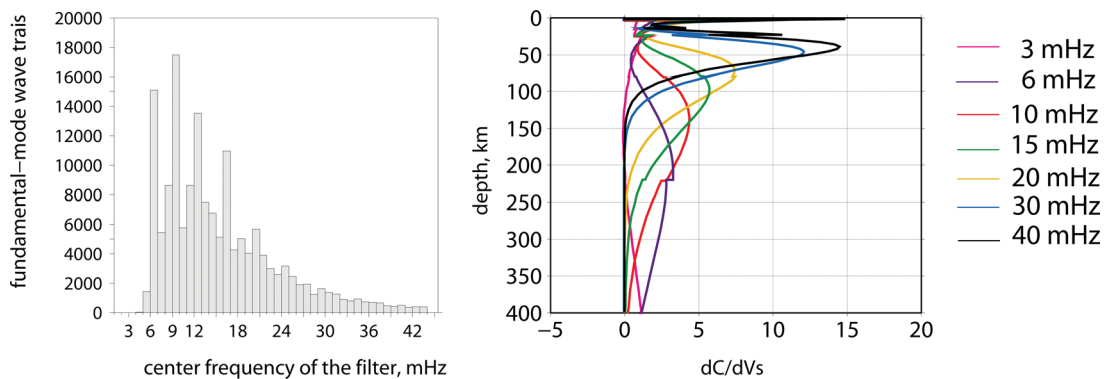


Figure 8. Left-hand panel: Histogram showing the distribution of fundamental-mode wave trains contributing to the inversion over the centre frequency of the bandpass filter. Right-hand panel: Sensitivity of the fundamental-mode, surface wave phase velocities to shear wave velocity perturbations at depth for selected frequencies.

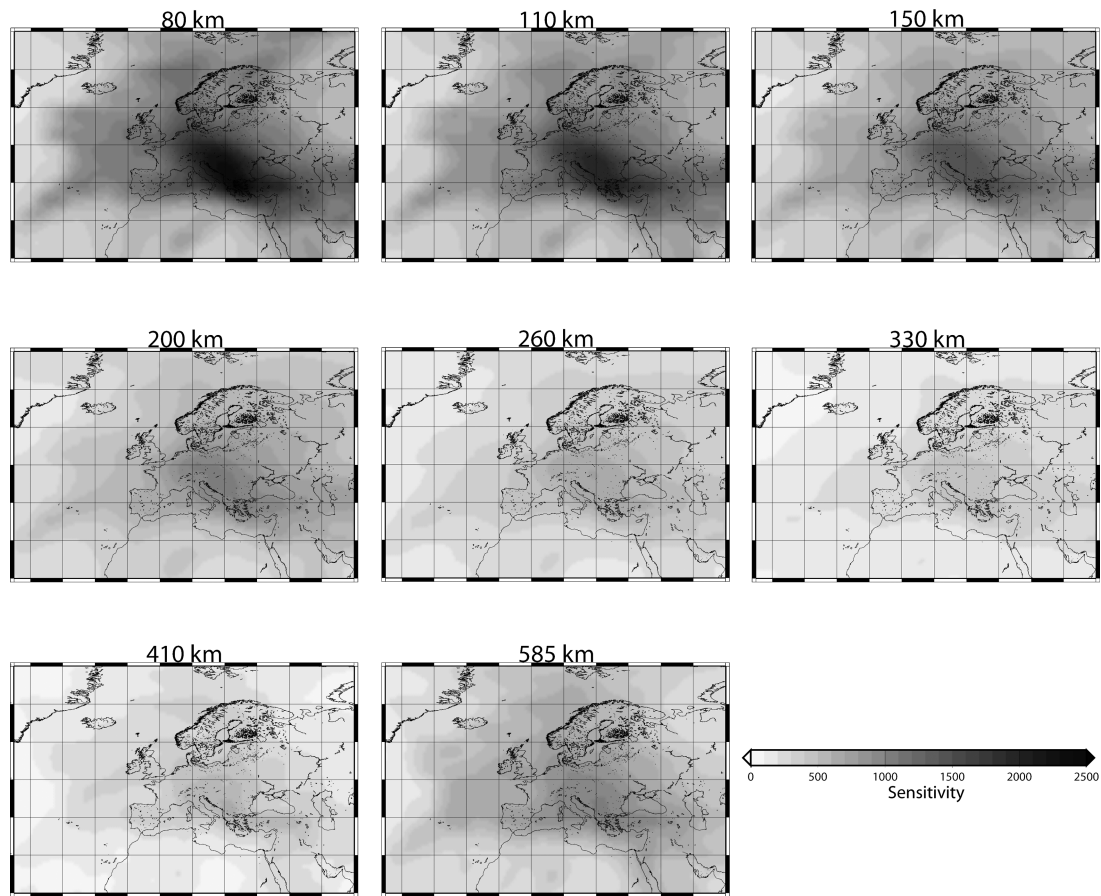


Figure 9. Sensitivity of the data vector to the velocity perturbation indicating the available constraints for different depths (from 80 to 585 km). The gray colour indicates a high amount of data, whereas the light colour represents a smaller amount of data. The colour scale is the same for each depth.

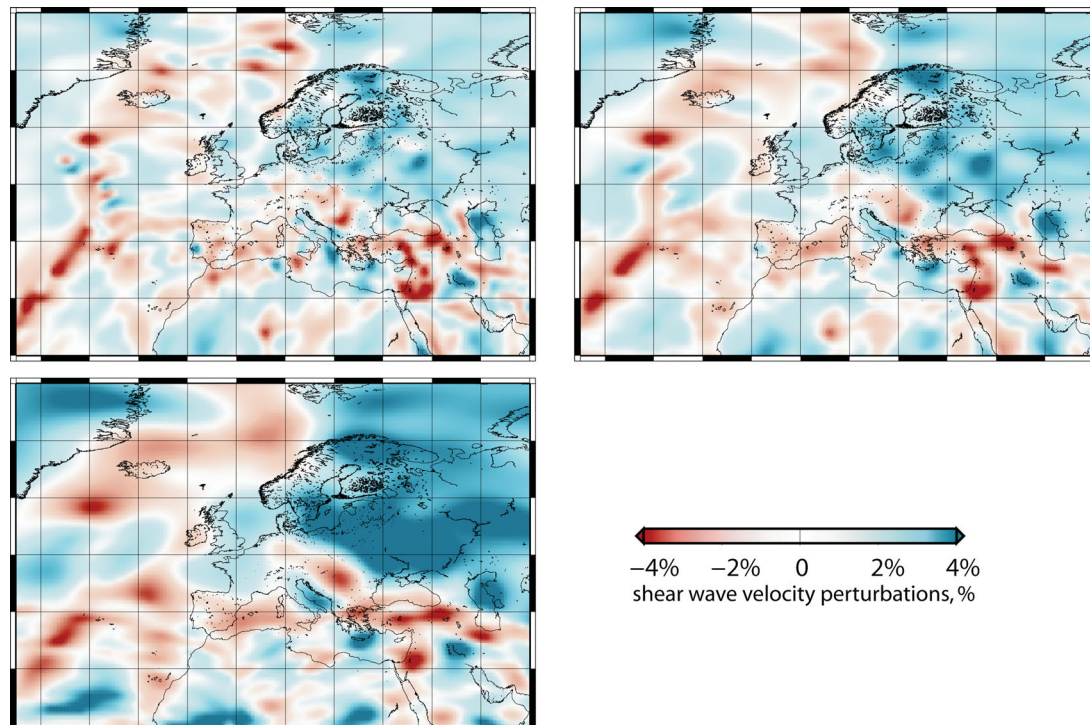


Figure 10. Effect of smoothing on the resulting velocity model at 110 km depth. Smoothing increases from top left to top right to bottom left.

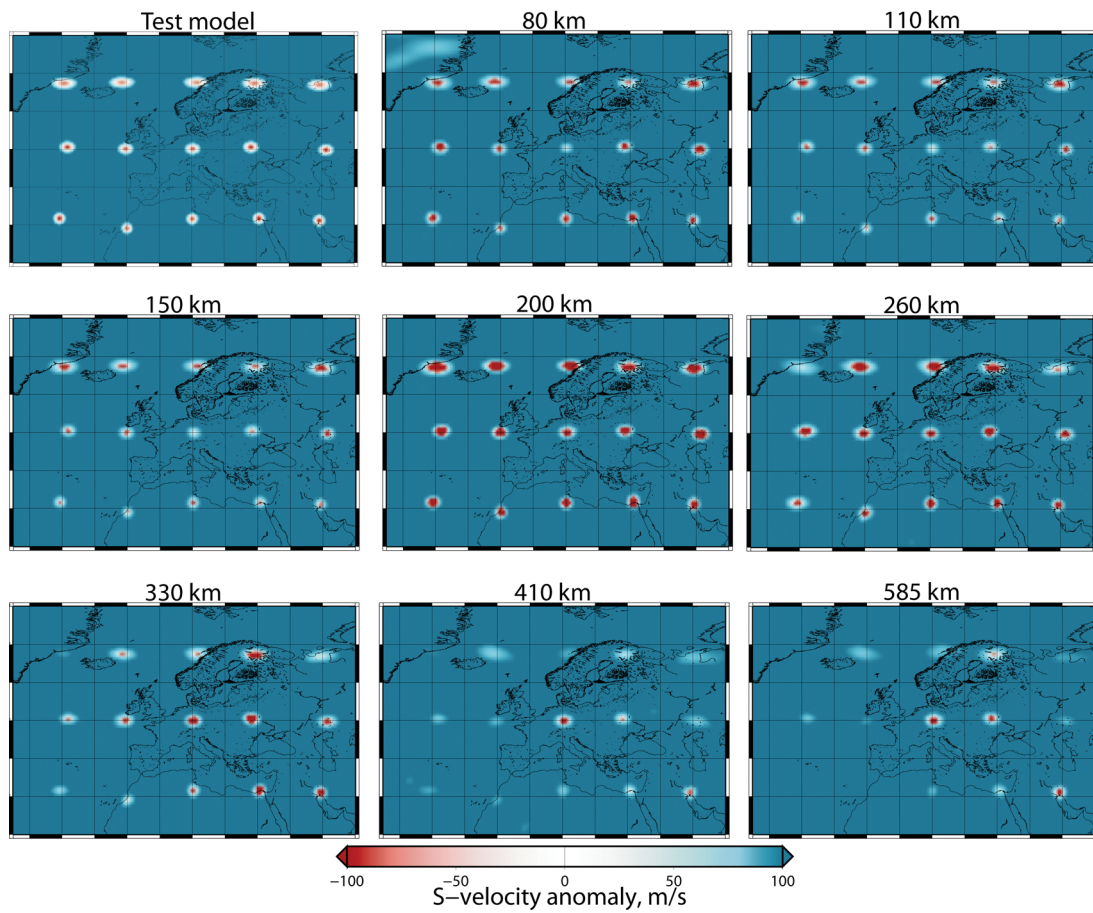


Figure 11. Resolution tests for the smooth version of the model: test models (top left) and reconstruction for different depths (80, 110, 150, 200, 260, 330, 410 and 585 km).

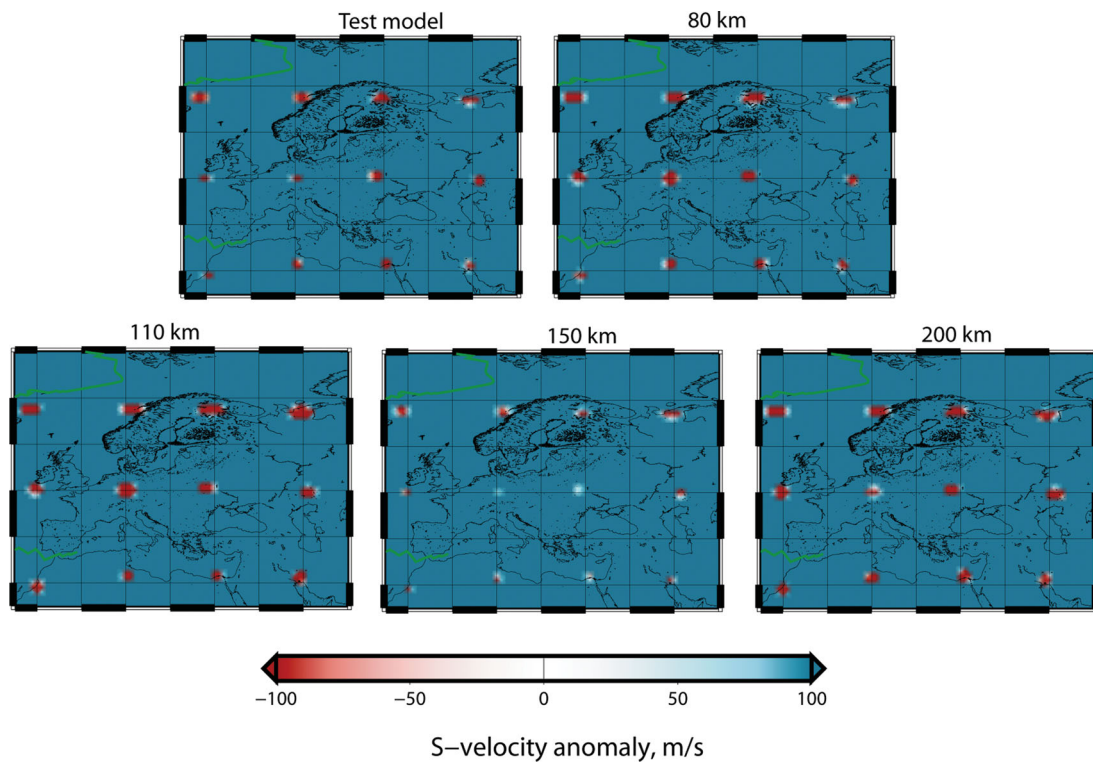


Figure 12. Resolution tests for the rough version of the model: test models (top-left image) and reconstruction for different depths (80, 110, 150 and 200 km).

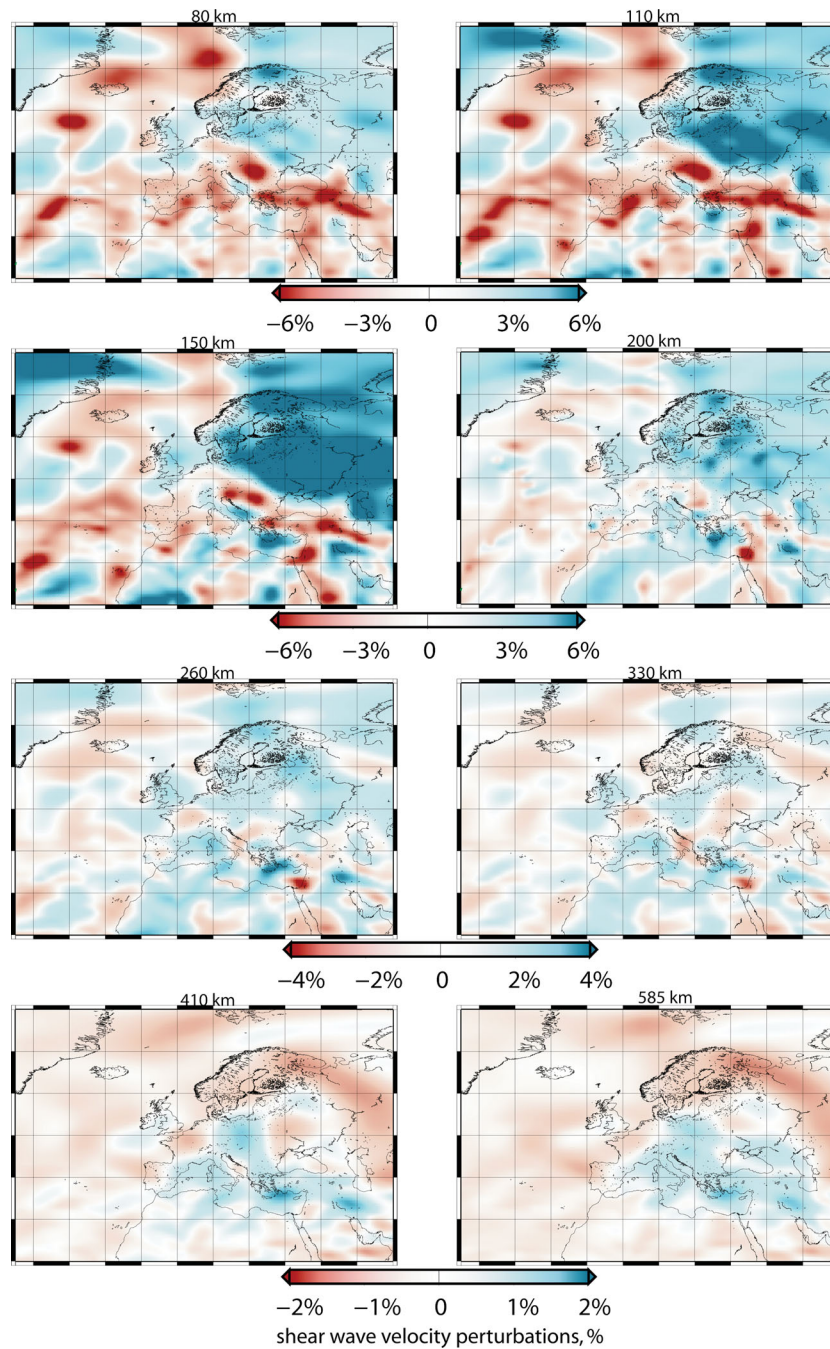


Figure 13. Model I. From top to bottom different horizontal slices are presented, at 80, 110, 150, 200, 260, 330, 410 and 585 km depths. These slices display a regional-scale, smooth S -velocity model for the European upper mantle and surroundings. The reference SV -wave velocity values are 4.38 km s^{-1} (at 80 and 110 km), 4.39 km s^{-1} (at 150 km), 4.45 km s^{-1} (at 200 km)—all at a reference period of 50 s. The reference SV -wave velocity values are 4.62 km s^{-1} (at 260 km), 4.75 km s^{-1} (at 330 km), 4.99 km s^{-1} (at 410 km), 5.34 km s^{-1} (at 585 km)—all at a reference period of 50 s.

Boschi *et al.* 2009; Lekić & Romanowicz 2011a,b; Schäfer *et al.* 2011). The EEC has also been imaged by global body wave studies as well (e.g. Bijwaard & Spakman 2000; Karason & van der Hilst 2000; Grand 2002; Amaru *et al.* 2008; Simmons *et al.* 2010).

The depth extent of the high velocities, interpreted as an indication of cratonic mantle lithosphere, has been a matter of debate (see, e.g. Kustowski *et al.* 2008). Our model I supports the findings of recent global and regional studies that reported high velocities down to about 200 km depth, with a distinct decrease of the perturbations below 200 km (Ritsema *et al.* 2004; Panning & Romanowicz

2006; Kustowski *et al.* 2008; Lebedev & van der Hilst 2008). The largest positive perturbations occur at around 150 km depth. Already at 260 km depth, a large-scale signal of the cratonic mantle lithosphere is absent. Below this depth, high velocities are present beneath parts of the craton as well as beneath parts of Phanerozoic continental Europe. The mantle transition zone beneath the EEC is characterized by lower than average velocities. That means there are no clear indications for a large-scale deep continental root with slightly increased velocities below the cratonic mantle lithosphere, as proposed by Kustowski *et al.* (2008).

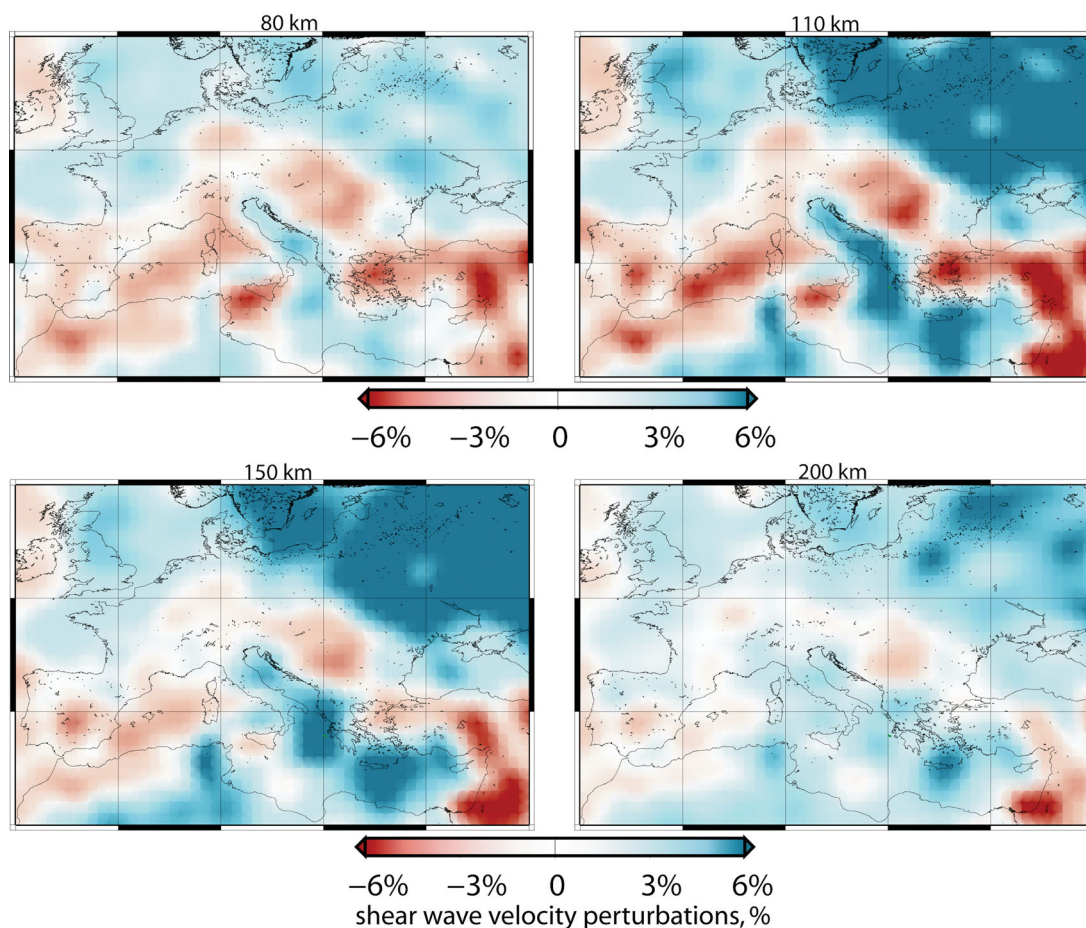


Figure 14. Model II. From top to bottom different horizontal slices are introduced, for 80, 110, 150 and 200 km depth. These slices show a detailed (rough), regional-scale velocity model for the European upper mantle. The reference SV -wave velocity values are 4.38 km s^{-1} (at 80 and 110 km), 4.39 km s^{-1} (at 150 km), 4.45 km s^{-1} (at 200 km)—all at a reference period of 50 s.

Our model also resolves lateral heterogeneity within the cratons. At 110–150 km depth an east–west trending region of reduced velocities within the cratonic mantle lithosphere, extending almost continuously from the Petchora Basin (PB) towards central Norway through Finland, is present in model I (Fig. 13, see Fig. 15 for a comparison to surface tectonics). Velocities within this region are still above the global average but lower than expected for cratonic mantle lithosphere. High-velocity regions in the northwest of the EEC and beneath the East European Platform in the SE of the craton are separated by this anomalous region. This east–west trending zone appears to be characterized by a smaller lithospheric thickness and underlain by low velocities below 300 km depth (Fig. 13). Domains of Archean crust within the EEC are indicated in Fig. 15 by pink dashed lines. From this comparison, it is obvious that these lateral variations in S -wave velocities within the mantle lithosphere are not correlated with variations in the age of the cratonic crust. This zone of reduced S velocities at 110–150 km depths runs through Proterozoic as well as Archean domains. Interestingly, diamond bearing kimberlites in the northwestern EEC (see Fig. 15) are found exclusively in this region of reduced seismic velocities in the mantle lithosphere and lower lithospheric thicknesses. The lower than expected velocities within the shallower cratonic mantle lithosphere may be indicative of metasomatism of the mantle lithosphere or changes in temperature. This alteration of the lithospheric structure may have been caused, at least partly, by the same events that gave rise to the eruption of the diamond bearing kimberlites. The ages

of the kimberlites are 490–600 Ma (Janse & Sheahan 1995). These ages would hint at Caledonian ages for a modification of the cratonic mantle lithosphere.

Bruneton *et al.* (2004) used data of the SVEKALAPKO experiment to derive a local 3-D model of the S -wave velocities in Finland, for depths between 70 and 150 km. Although the scale of their study was smaller, the main features of their model are supported by model I (Fig. 13), especially the east–west trending low-velocity anomaly in the shallower mantle lithosphere at about 100 km depth and the higher velocities beneath the Finnish Archean Shield at about 150 km depth.

The east–west trending zone of reduced velocities also seem to be related to a similarly oriented region of increased heatflow of about $40 \times 10^{-3} \text{ W m}^{-2}$, compared to a heat flow of about $20 \times 10^{-3} \text{ W m}^{-2}$ in neighbouring regions (see, e.g. Artemieva 2007). A similar zone of reduced P -wave velocities can be found in the global model of Bijwaard *et al.* (1998) at 200 km depth. The internal structure of the mantle lithosphere of the EEC, as revealed by model I (Fig. 13), points to considerable changes in its temperature and/or composition after the formation of the craton.

Model I also resolves in detail the northwestern and southwestern margins of the EEC (Fig. 15). The northwestern margin of the EEC along the Norwegian coastline has been influenced by the Caledonian Orogeny and, subsequently, by the opening of the North Atlantic. In Fig. 15, the coastline of Greenland at 50 Ma—at the beginning of the opening of the northern Atlantic—is plotted (in

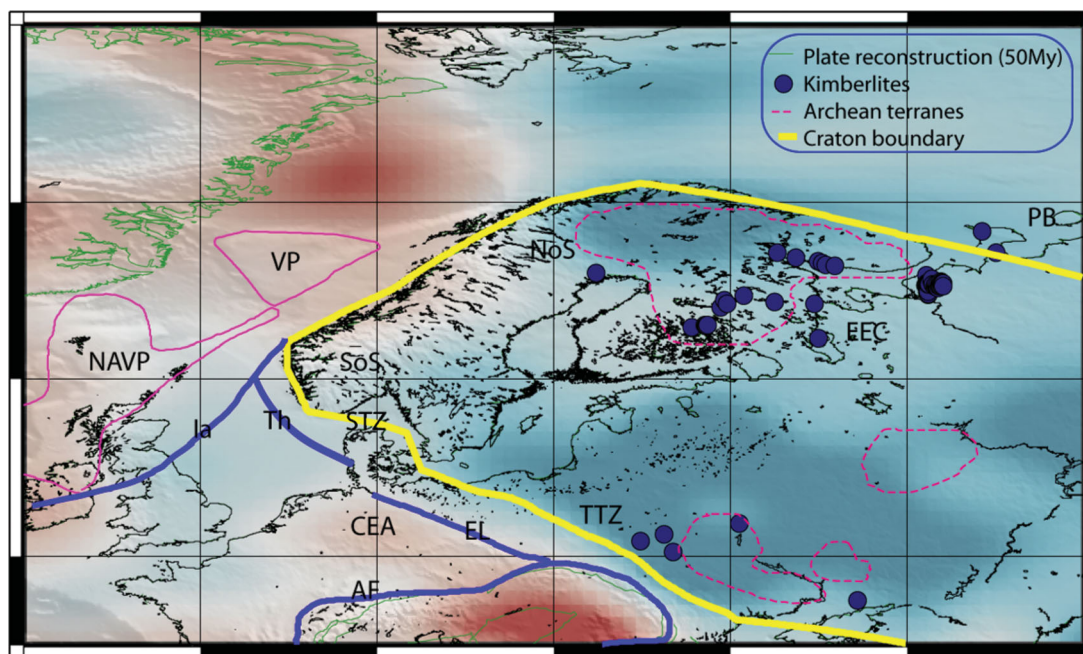


Figure 15. Structural interpretation of model I at 110 km depth in the region of the East European Craton. The map presents some tectonic structures (AF, Alpine Front; CEA, Central European Asthenosphere; EEC, East European Craton; EL, Elbe Line; Ia, Iapetus Suture; NAVP, North Atlantic Volcanic Province; NoS, Northern Scandies; PB, Petchora Basin; SoS, Southern Scandies; STZ, Sorgenfrei-Tornquist Zone; Th, Thor Suture; TTZ, Tornquist-Teisseyre Zone; VP, Vøring Plateau). In addition, the location of diamond bearing kimberlites (blue dots) as well as the boundaries of the Archean crustal domains within the cratons (dashed pink line), and the plate reconstruction at 50 Ma with respect to an European reference frame (PLATES software: <http://www.ig.utexas.edu/research/projects/plates/>) are given (green lines).

green) in a Eurasia-fixed reference frame, on top of the model I at 110 km depth (the Eurasian coastline is present-day). The low velocities in the North Atlantic at this depth extend to beneath southwestern Scandinavia, where a mantle source for the Neogene uplift of the Scandes has been suggested by Rohrman & van der Beek (1996). This view is consistent with residual topography being supported by the sublithospheric mantle (Artemieva 2007). A local surface wave study by Weidle & Maupin (2008) indicates that the mantle lithosphere here is similar to the lithosphere in Denmark but different from cratonic lithosphere. The shape of the low-velocity area in model I, extending from the Atlantic to beneath western Scandinavia (Fig. 15), points to the erosion of the Eurasian mantle lithosphere by the asthenosphere of the northern Atlantic. The erosion seems to be stronger between the northern and southern Scandes (NoS and SoS in Fig. 15). The low velocities at 110 km depth in the region of the Scandes may be related to the opening of the northern Atlantic and to an approximately 2000-km-wide region of elevated temperatures that may have existed prior to rifting, as postulated by White (1988).

It is interesting that the low velocities west of the EEC are more pronounced northeast of the Vøring Plateau (it is denoted by VP in Fig. 15) compared to the anomaly directly beneath the volcanic plateau itself. The Vøring Plateau (VP) is a part of the North Atlantic Volcanic Province (NAVP) that formed prior to the development of the North Atlantic mid-ocean ridge. It comprises an about 58-Myr-old central volcano and has been thickened by magmatic underplating (Rohrman & van der Beek 1996). Heat and possibly melts may have already been extracted, at least partly, from the asthenosphere beneath the VP by magmatism, whereas the strong low-velocity anomaly northeast of it may indicate increased temperatures and melts, still present in the North Atlantic asthenosphere.

The southwestern margin of the EEC in Poland is indicated, at the surface, by the TTZ. From Figs 15 and 16, it is obvious that the TTZ in Poland marks, also, the southwestern boundary of the high *S*-wave velocities at 110–150 km depths beneath the East European Platform, as has been noted before (e.g. by Zielhuis & Nolet 1994). Northeast of the TTZ, the craton has been stable since the Proterozoic.

Models I and II also show moderately high velocities between the Elbe Line (EL) and the TTZ that are clearly lower than those in the cratonic mantle lithosphere but higher than the low velocities of the Central European Asthenosphere (CEA). This can be seen for model I in Figs 13 and 15 and for model II in Figs 14 and 16. Based on seismic receiver function, body wave and surface wave studies, it has already been suggested that both the EL and the TTZ mark strong lateral changes in the lithospheric structure (Ansorge *et al.* 1992; Meier *et al.* 1997a; Arlitt *et al.* 1999; Gossler *et al.* 1999; Scheck *et al.* 2002; Shomali *et al.* 2002; Gregersen *et al.* 2010). Here, we image a zone with distinct lithospheric seismic-velocity structure between the EL and TTZ, extending from the North German Basin (NGB) to southeastern Poland (Fig. 16).

5.2 Central and western Europe

The zone of moderately increased velocities at 110 km depth extends beneath the North Sea and much of Britain, and towards the Paris Basin. In the following and in Fig. 16, we refer to this zone as the western European continental mantle lithosphere (WECML). It has been resolved, in part, by Boschi *et al.* (2009) and Schäfer *et al.* (2011). They combined surface wave phase velocity measurements by Fry *et al.* (2008) and Boschi *et al.* (2009) to compute global models, with a focus on and higher resolution in the central

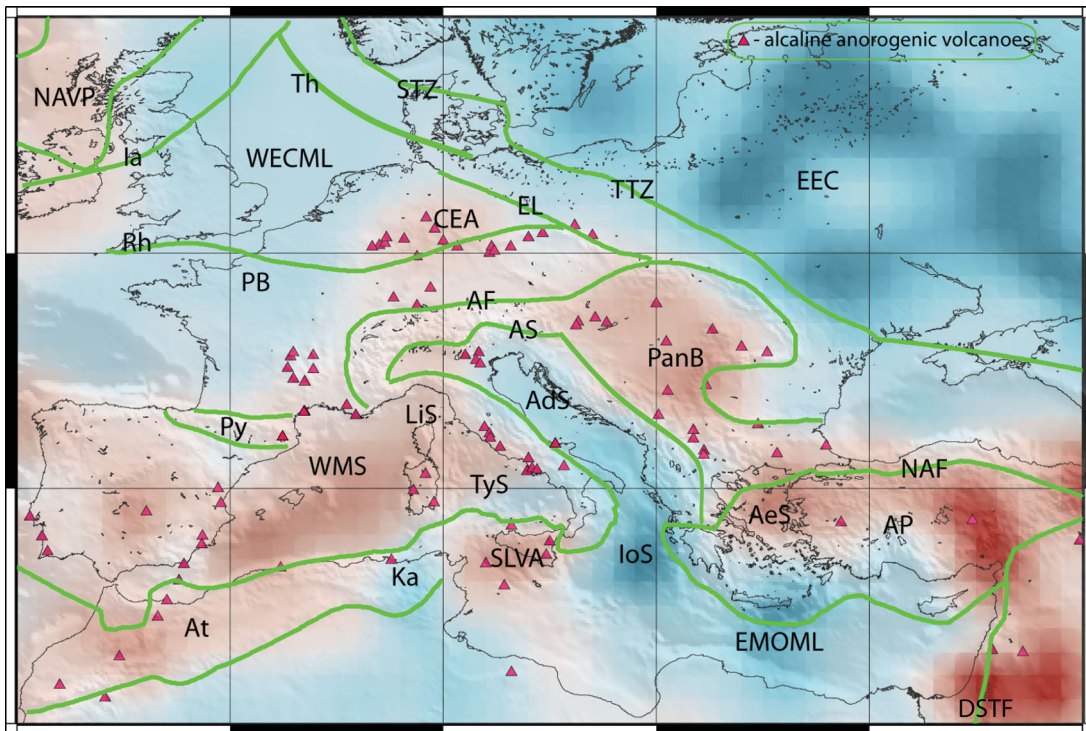


Figure 16. Structural interpretation for central Europe and the circum Mediterranean (model II). Tectonic features (AdS, Adriatic Sea; AeS, Aegean Sea; AF, Alpine Front; AP, Alpine Plateau; AS, Alpine Suture; At, Atlas Mountains; CEA, Central Europe Asthenosphere; DSTF, Dead Sea transform fault; EEC, East European Craton; EL, Elbe Line; EMOML, eastern Mediterranean oceanic mantle lithosphere; Ia, Iapetus Suture; IoS, Ionian Sea; Ka, Kabyllies; LiS, Ligurian Sea; NAF, North Anatolian Fault; NAVP, North Atlantic Volcanic Province; PanB, Pannonian Basin; PB, Paris Basin; Py, Pyrénées; Rh, Rhenic Suture; SLVA, Sicilian low-velocity anomaly; STZ, Sorgenfrei-Tornquist Zone; Th, Thor Suture; TyS, Tyrrhenian Sea; WECML, west European continental mantle lithosphere; WMS, western Mediterranean Sea) on top of the model II at 110 km depth. Alkaline anorogenic volcanoes are also indicated (see text for further explanations).

European upper mantle. There is a good agreement between their model and model II with respect to the extent of the WECML beneath the North Sea, Britain and northern France (Fig. 16). The WECML is also visible in the model presented by Chang *et al.* (2010) who jointly inverted traveltimes, group velocities and waveforms.

Large parts of the Caledonian Iapetus (Ia) and Thor (Th) Sutures are located within this region of rather homogeneous mantle lithosphere. In Fig. 16, these sutures are indicated on a mapview of model II at 110 km depth. Consequently, these sutures do not mark large-scale lateral changes in the mantle lithosphere (neither here nor to the west, beneath Ireland and the Irish Sea, where seismic velocities are lower). We conclude that the first-order properties of the WECML are likely to have been determined by post-Caledonian lithospheric evolution. An alternative interpretation could be that plates with similar properties of the mantle lithosphere collided and that the mantle lithosphere remained unaltered. However, three different plates—Avalonia, Baltica and Laurentia—are joined together by these sutures and, also, it is unlikely that the mantle lithosphere survived unaltered subduction processes prior to collision, the Caledonian orogeny, post-orogenic collapse, and the intense Permian volcanism (see, e.g. Blundell *et al.* 1992). Therefore, we interpret the finding of a laterally homogeneous WECML as an indication for strong post-orogenic alteration and homogenization of the mantle lithosphere. At 110 km depth, the WECML borders the CEA that displays substantially lower velocities (Fig. 16). In agreement with previous studies on the lithosphere–asthenosphere boundary

(LAB) in central Europe (e.g. Plomerová *et al.* 2007; Babuška *et al.* 2010; Geissler *et al.* 2010), these low velocities indicate lower thicknesses of the lithosphere in central Europe (<100 km). Plomerová & Babuška (2010) reported a lithospheric thickness of about 60 km in the North Sea region, which does not agree with our results (thickness of about 100 km). We note, however, that due to a lack of stations in this region, some small-scale heterogeneity in the North Sea might not be resolved by our model.

According to model II, the boundary between the WECML and the CEA at 110 km depth does not follow the Rhenic Suture between Avalonia in the north and the Saxothuringian terranes south of it (Fig. 16). On the contrary, the WECML seems to extend towards the Paris Basin, into the Saxothuringian and American terranes. Therefore, the WECML is not confined to Avalonia and, at least in the Variscan domains, it is very likely of post-Variscan age.

The lower thicknesses of the lithosphere in central, compared to western, Europe point to differences in the post-Variscan evolution of the mantle lithosphere between them. The uniformly high S-wave velocities across the WECML are probably a result of post-Caledonian and post-Variscan processes. We interpret this as evidence for cooling of the mantle lithosphere since at least the Permian, the time of the last large-scale heating of the western European mantle lithosphere, as indicated by widespread volcanism at that time (e.g. Ziegler 1986; Doblas 1998; Heeremans *et al.* 2004; Timmerman *et al.* 2009). The rather flat Moho in the region supports our interpretation. We note, however, that according to controlled-source seismic investigations heterogeneity in the crust,

and especially in the upper crust, has remained strong within and between the different tectonic domains.

Remarkably, the mantle lithosphere beneath Ireland is distinctly different from the WECML, with low velocities found beneath Ireland and the Irish Sea between 80 and 200 km depth. The voluminous volcanism in northern Ireland is considered a part of the NAVP (White 1988; White & Lovell 1997; Arrowsmith *et al.* 2005). The low velocities beneath Ireland—the western extremity of Europe—may be related to the opening of the North Atlantic, the Iceland Hotspot activity and episodic Cenozoic magmatism in the region (Rohrman & van der Beek 1996; Wawerzinek *et al.* 2008; O'Donnell *et al.* 2011; Polat *et al.* 2012).

We compiled the locations of Cenozoic anorogenic alkaline volcanism in central and western Europe and the circum Mediterranean, based mainly on Wilson & Downes (1991), Wedepohl & Baumann (1999), Harangi *et al.* (2006), and Lustrino & Wilson (2007). These locations are indicated in Fig. 16 which shows the model II at 110 km depth. Cenozoic anorogenic volcanism is almost exclusively found in regions of low velocities at 80–200 km depth or close to transitions from high to low velocities at 110 km depth. The only exception may be the region in Upper Silesia between the EL and the TTZ. For central Europe, the relation between the CEA and the Cenozoic volcanism has already been noted by Hoernle *et al.* (1995), using a lower resolution tomographic model. This finding remains valid for our high-resolution model II. Based on local studies, Granet *et al.* (1995) and Sobolev (1997) found that the volcanism in the Massif Central occurs in a region of thin lithosphere and above a plume-like structure that extends down to about 300 km depth. Similar observations are reported for the Eifel Hotspot (Ritter *et al.* 2001; Kaiser *et al.* 2005; Mathar *et al.* 2006). For the Eger Rift, Plomerová *et al.* (2007) infer an upwelling of the asthenosphere–lithosphere transition without any plume like structure. From our model II (Fig. 16), we can conclude that the Cenozoic volcanism in central and western Europe is located in an interconnected region of thin lithosphere above a shallow asthenosphere. The Cenozoic volcanism in Spain is also located in a region of similar properties. However, the asthenosphere beneath Spain seems to be disconnected from the CEA by a high-velocity anomaly beneath the Pyrenees, probably related to subduction (Souriau *et al.* 2008). In the Euro–Mediterranean region, all areas with thin lithosphere and shallow asthenosphere are, thus, characterized by anorogenic volcanism. This volcanism may be caused by upwards directed flow of asthenosphere or sub-horizontal flow of the asthenosphere along the LAB of varying depth, with decompression melting when asthenospheric material ascends (Thompson & Gibson 1991; Lebedev *et al.* 2006). In the region of the Massif Central, the low velocities extend down to the bottom of our model in the transition zone (see model I, Fig. 13) supporting the view by Faccenna & Becker (2010) that this region is characterized by upwelling in the entire upper mantle. In contrast, continental areas without Cenozoic volcanism show higher velocities at 110 km depth, indicating thicker lithosphere. That implies that the cooling of continental lithosphere leads either to the freezing of former magma reservoirs, or to the cessation of decompression melting episodes beneath the now-thicker lithosphere.

5.3 The Mediterranean region

The highest resolution of the upper mantle in the Mediterranean has been achieved, so far, by *P*-wave velocity models (Bijwaard & Spakman 2000; Piromallo & Morelli 2003). Here, we add high-resolution

upper-mantle *SV*-wave models, based on automated waveform inversions that sampled the entire Mediterranean. The upper mantle in the area has been the target of a number of tomographic surface wave and waveform studies (e.g. Boschi *et al.* 2004; Marone *et al.* 2004a; Panza *et al.* 2007; Peter *et al.* 2008; Schmid *et al.* 2008; Boschi *et al.* 2009; Chang *et al.* 2010), with probably the highest resolution to date in the models by Boschi *et al.* (2009) and Chang *et al.* (2010). Our models confirm the main features of this model and show a comparable or even higher resolution. In general, the resolution of the lithosphere–asthenosphere system is higher in model II than in previous studies but resolution of slab segments in the Mediterranean is lower than in recent *P*-wave velocity models. At shallow depths of 80 km and 110 km (Figs 14 and 16), low *S*-wave velocities beneath the Atlas Mountains (At), the Ligurian Sea (LiS), beneath Sicily (Sicilian low-velocity anomaly, SLVA), the Pannonian Basin (PanB), the Northern Aegean (AeS), Turkey and the Middle East are in contrast with high velocities beneath the Kabylies (Ka), the Adriatic and Ionian Seas (AdS, IoS) and the eastern Mediterranean. We discuss some of these features briefly in the following.

A broad low-velocity anomaly underlies the At, with the lowest velocities beneath the Middle Atlas (Fig. 16). The anomaly is located beneath the sites of the Neogene intracontinental volcanism in the At (Ayarza *et al.* 2005; Duggen *et al.* 2009). A channel towards the Canary region as proposed by Duggen *et al.* (2009), following the Terceira Rift (Beier *et al.* 2008) from the At towards the east to the Madeira and Canary is supported by our model I (see Fig. 13 at depths between 80 and 200 km). To the east, this zone of low velocities terminates beneath the Kabylies. The presence of a high-velocity anomaly in this region, as also seen in other recent high-resolution models (Bijwaard & Spakman 2000; Piromallo & Morelli 2003; Boschi *et al.* 2009), is confirmed by our tomography, although the anomaly's shape remains somewhat uncertain as it is considerably different in these models.

At upper-mantle depths, a low-velocity anomaly directly beneath Sicily—the SLVA—separates the slab-related high velocities beneath the Tyrrhenian Sea from high velocities indicating the Ionian mantle lithosphere (IoS, see Fig. 16). The SLVA probably shows the mantle domain that is the deep source of the Sicilian volcanism. This is in agreement with geochemical data: Etna is an intraplate volcano with magmas of an Oceanic Island Basalt (OIB) character. Only in geologically recent times, minor geochemical indications of subduction signature began to appear (Beccaluva *et al.* 2007; Lustrino & Wilson 2007).

In the eastern Mediterranean Sea, high velocities down to about 150 km depth indicate an old-oceanic character of the lithosphere of the IoS, east of the Calabrian Arc, as well as of that south of the eastern Aegean and western Turkey. In Fig. 16, we refer to the latter high-velocity anomaly as eastern Mediterranean oceanic mantle lithosphere (EMOML). These two regions are separated by mantle lithosphere with lower velocities, identified previously in a local study by Meier *et al.* (2004). As already indicated by, for example Bijwaard & Spakman (2000), Erduran *et al.* (2008) and Boschi *et al.* (2009), the oceanic lithosphere in the eastern Mediterranean (EMOML) seems to extend towards Cyprus but not further east. At 110 km depth, the mantle lithosphere of the Apulian indenter is imaged beneath the entire Adriatic Sea (AdS in Fig. 16). At 150 km, the velocities in the Adriatic Sea are lower, however, than those of the oceanic lithosphere of the IoS, indicating differences in lithospheric properties between the AdS and IoS.

The low velocities at 80–150 km depths beneath the western Mediterranean Sea (WMS), the PanB and the Northern Aegean

Sea (AeS) are quite similar in amplitudes (see Figs 14 and 16), indicating pronounced shallow asthenosphere in these backarc settings (e.g. Wortel & Spakman 2000). Fig. 16 shows that the North Anatolian Fault (NAF) is located in the vicinity of a strong lateral change in upper-mantle *S* velocities, from high in the north to low in the south, beneath Turkey (Villaseñor *et al.* 2001b; Faccenna *et al.* 2006). Low velocities found beneath the Anatolian Plateau (AP) at 110 km depth (Fig. 16) are consistent with previous studies (Villaseñor *et al.* 2001b; Faccenna *et al.* 2006; Boschi *et al.* 2009; Chang *et al.* 2010). Note, however, that beneath central Anatolia *S* velocities are increasing at greater depths, so that positive perturbations are found there below about 150 km depth (Fig. 14). This means that, in contrast to East Anatolia, the asthenospheric low-velocity anomalies in this region seem to be confined to depths shallower than about 150 km.

One of the most prominent features that are revealed by our models is a remarkable low-velocity anomaly at shallower upper-mantle depths (down to 200 km) extending from eastern Turkey towards the Dead Sea transform fault (DSTF) and Sinai, as can be seen most clearly in Fig. 14 and 16. Also in this region, we note a high correlation of low upper-mantle velocities with the locations of recent volcanism (Fig. 16). The DSTF is located above a shallow asthenosphere, characterized by very low *S* velocities (Debayle *et al.* 2001; Sebai *et al.* 2006; Pasyanos & Nyblade 2007; Erduran *et al.* 2008; Chang & van der Lee 2011).

Below 200 km depth, the amplitude of the *S*-wave heterogeneity in model I (Fig. 13) is decreasing significantly from over 6 per cent above 200 km to 2 per cent below. Between 260 and 410 km, the resolution of the *P*-wave models by Bijwaard & Spakman (2000) and Piromallo & Morelli (2003) is higher than that of model I, in particular near subduction zones, where the density of sources and stations is high. However, there is substantial agreement between the locations of slabs, as described, for example, by Spakman & Wortel (2004), Faccenna *et al.* (2004) and Handy *et al.* (2010), and corresponding anomalies in model I (Fig. 13). The most remarkable feature of our model at these depths is a laterally narrow low-velocity anomaly beneath Sinai and the Dead Sea, extending down to the transition zone. Chang & van der Lee (2011) observe a plume-like, low-velocity anomaly in the lower mantle beneath north-central Arabia that is located to the northeast of the vertical upper-mantle low-velocity anomaly in model I beneath Sinai and the Dead Sea.

The map views at 410 and 585 km depths show that the inversion of *S*- and multiple *S*-waveforms ensures a high lateral resolution in the transition zone—lower than at shallower depth but sufficient for structures with a lateral extent of only a few hundred kilometres to be resolved. In the Mediterranean, the high velocities in the transition zone are linked to subduction zones at the surface; in agreement with previous studies (e.g. Bijwaard & Spakman 2000; Faccenna *et al.* 2004; Spakman & Wortel 2004; Cloetingh *et al.* 2007; Handy *et al.* 2010), we interpret these as segments of subducted oceanic lithosphere. Spakman & Wortel (2004), Faccenna *et al.* (2004) and Handy *et al.* (2010) provide a detailed discussion on the transition-zone heterogeneity in the western Mediterranean. We note that in the eastern Mediterranean vertical tearing (de Boorder *et al.* 1998; Wortel & Spakman 2000; Meier *et al.* 2007; Brun & Sokoutis 2010), as well as segmentation of the slab in the direction of subduction (Meier *et al.* 2004; van Hinsbergen *et al.* 2005; Jolivet *et al.* 2009), are also expected. The high velocities in the transition zone beneath the eastern Mediterranean are, very likely, caused by different segments of subducted oceanic lithosphere. In agreement with Bijwaard & Spakman (2000), Piromallo & Morelli (2003) and

Dando *et al.* (2011), we report positive velocity perturbations in the transition zone beneath the PanB. The *S*-wave perturbations in our models are smaller, however: only about 1 per cent compared to up to 2 per cent perturbations in *P*-wave velocity.

Model I (Fig. 13) also shows positive perturbations in the transition zone beneath Poland. There are considerable variations between different models for this region. Low-velocity perturbations are found here by Boschi *et al.* (2009). No large-scale anomaly is present in the model by Piromallo & Morelli (2003). But there are high velocities at depths of around 300 km in the local model by Arlitt *et al.* (1999). Interestingly, magnetotelluric studies (Korja 2007) do not detect low-resistivity asthenosphere in the region. The apparent several-hundred-kilometres depth of the LAB, as suggested by Korja (2007) for this region, might be related to this high-velocity structure in the lower upper mantle. It could indicate a downwelling or, possibly, remnants of ancient subducted slabs.

5.4 The northern and central Atlantic

Regional tomographic studies have provided abundant evidence for large-scale low-velocity anomalies in the upper mantle beneath the North Atlantic, elongated in the direction of the Mid-Ocean Ridge (MOR: Mocquet *et al.* 1989; Shen *et al.* 1996; Helmberger *et al.* 1998; Silveira & Stutzmann 2002; Shen *et al.* 2002; Pilidou *et al.* 2005). Based on tomographic models of Ritsema *et al.* (1999) and Grand (2002), Conrad *et al.* (2004) showed that the dynamic topography of the North Atlantic is likely to be related to lower mantle heterogeneity and, in the region of Iceland, also to upper-mantle structure. Even though the northern Atlantic is located at the western margin of model I (Fig. 13), some main upper-mantle features are well resolved, including the broad, low-velocity anomalies at 80 km depth beneath the MOR. In some locations, they extend down to 200 km depth, and in the region of Iceland they reach depths of 300 km. In the transition zone, Iceland seems to be surrounded by low velocities.

Amplitudes of low velocities vary considerably along the MOR. In most of the MOR, pronounced low-velocity anomalies are found, especially below the active volcanoes (Iceland) and north of the Charlie-Gibbs Fracture Zone, where active volcanism is observed (Silveira & Stutzmann 2002; Barclay & Toomey 2003; Pilidou *et al.* 2005; Lustrino & Wilson 2007). In contrast, the Charlie-Gibbs Fracture Zone (located around 53°N and −35°W and representing a system of transform faults associated with a large lateral offset of the Mid Atlantic Ridge) is characterized by slight positive velocity anomalies down to 150–200 km (+2 per cent at 150 km and +1 per cent at 200 km) but not deeper. Interestingly, the relatively high velocities in the region of the transform system correspond to reduced magma upwelling as reported by Lonsdale & Shor (1979).

In the region of the Azores and Madeira hotspots in the central Atlantic, model I (Fig. 13) indicates rather complicated structures down to about 150 km depths. Only the Canaries hotspot seems to be related to a narrow vertical low-velocity anomaly that extends into the transition zone.

6 CONCLUSIONS

We have assembled all available waveforms recorded at permanent and temporary broad-band stations in Europe for events in and around Europe for the time period between 1990 and 2007. In addition, recordings for events at larger distances for the years 1995 and 1996 have been added. AMI proved to be a highly efficient

tool for waveform inversion of large data sets. Rayleigh and *S*-waveforms from about 78 000 seismograms provided about 320 000 linear equations that constrain our *S*-velocity model of European upper mantle. Highly rigorous rejection criteria were used to focus on the high-quality data that could provide the best constraints on our tomographic inversion. Due to a dense data coverage, the lateral resolution of our models is in the order of the wavelength of the waves used in the inversion. It is about 150 km at shallow upper-mantle depths and about 400 km in the mantle transition zone.

Major findings of our study are: In the region of the EEC, the strongest high-velocity anomaly occurs at about 150 km depth. Below 150 km, the velocity anomaly is significantly decreasing with depth. High velocities at 260 km are no longer clearly related to the boundaries of the craton at the surface. Only in some regions of the craton high velocities are found down to about 330 km depth.

Diamond bearing kimberlites occur in regions with lower than expected *S*-wave velocities in the upper cratonic mantle lithosphere at about 110 km depth. This observation hints at substantial metasomatism and/or changes in temperature in the cratonic mantle lithosphere associated with volcanic events after the formation of the craton.

At the western margin of the EEC beneath the Scandes, low-velocity anomalies point to erosion of the cratonic mantle lithosphere by asthenosphere of the northern Atlantic.

Like the TTZ that marks the southwestern border of the cratonic mantle lithosphere, the EL is associated with strong lateral changes in properties of the mantle lithosphere. Slightly increased *S*-wave velocities at 80–150 km depth between the TTZ and the EL point to continental mantle lithosphere cooling at least since the Permian.

The Caledonian and Variscian sutures are not related to strong lateral changes in the current central European lithosphere–asthenosphere system. Therefore, the mantle lithosphere and the asthenosphere in central Europe are very likely of post-Variscian age.

Intraplate anorogenic volcanism is almost exclusively found in regions of shallow asthenosphere and in areas where the depth of the LAB changes significantly.

Low-velocity zones extending from shallow upper-mantle depths down to the mantle transition zone are found beneath the Massif Central, Sinai and the Dead Sea, the Canary Islands, and Iceland. High *S*-wave velocities in the transition zone are found beneath the Mediterranean, the PanB and beneath the North German-Polish Trough.

ACKNOWLEDGMENTS

The authors wish to thank Ved Lekic and Stewart Fishwick for their constructive reviews.

This work was funded by the German Science foundation grants DFG-FR1146/7-1. It was an associated project of the Topo-Europe project Topo-4D. Furthermore, it was partly supported by the Collaborative Research Center 526 ‘Rheology of the Earth—from the upper crust to the subduction zone’ at Ruhr-University Bochum and by the Science Foundation Ireland grant 08/RFP/GEO1704 and 09/RFP/GEO2550. Waveform data were obtained from facilities of the IRIS Data Management System (DMS), GEOSCOPE, ORFEUS, GEOFON Program (GFZ Potsdam) and the RéNaSS.

We thank the EGELADOS working group for sharing data and the GIPP (Geophysical Instrument Pool Potsdam (GIPP) at Geoforschungszentrum (GFZ) Potsdam) for providing portable seismic instruments. Figures were generated with Generic Mapping Tools (Wessel & Smith 1995).

REFERENCES

- Aki, K., Christofferson, A. & Husebye, E., 1977. Determination of the three-dimensional seismic structure of the lithosphere, *J. geophys. Res.*, **82**, 277–296.
- Alsina, D. & Snieder, R., 1996. Constraints on the velocity structure beneath the Tornquist-Teisseyre Zone from beam-forming analysis, *Geophys. J. Int.*, **126**, 205–218.
- Amaru, M.L., Spakman, W., Villaseñor, A., Sandoval, S. & Kissling, E., 2008. A new absolute arrival time data set for Europe, *Geophys. J. Int.*, **173**, 465–472.
- Ansorge, J., Blundell, D.R. & Mueller, S., 1992. *A Continent Revealed: The European Geotraverse*, Vol. 3, Cambridge University Press, Cambridge.
- Arlitt, R., Kissling, A., Ansorge, J. & TOR Working Group, 1999. Three-dimensional crustal structure beneath the TOR array and effects on teleseismic wavefronts, *Tectonophysics*, **314**, 309–319.
- Arrowsmith, S.J., Kendall, M., White, N., Vandecar, J.C. & Booth, D.C., 2005. Seismic imaging of a hot upwelling beneath the British Isles, *Geology*, **33**, 345–348.
- Artemieva, I.M., 2007. Dynamic topography of the East European Craton: shedding light upon lithospheric structure, composition and mantle dynamics, *Glob. planet. Change*, **58**(1–4), 411–434.
- Ayarza, P., Alvarez-Lobato, F., Teixell, A., Arboleya, M.L., Tesón, E., Julivert, M. & Charroud, M., 2005. Crustal structure under the central High Atlas Mountains (Morocco) from geological and gravity data, *Tectonophysics*, **400**, 67–84.
- Babuška, V., Fiala, J. & Plomerová, J., 2010. Bottom to top lithosphere structure and evolution of western Eger Rift (central Europe), *Int. J. Earth Sci.*, **99**, 891–907.
- Barclay, A. & Toomey, D., 2003. Shear wave splitting and crustal anisotropy at the Mid-Atlantic Ridge, 35°N, *J. geophys. Res.*, **108**(2378), 1–10.
- Bassin, C., Laske, G. & Masters, G., 2000. The current limits of resolution for surface wave tomography in North America, *EOS, Trans. Am. geophys. Un.*, **81**, F897.
- Beccaluva, L., Bianchini, G., Wilson, B. & Wilson, M., 2007. *Cenozoic Volcanism in the Mediterranean Area*, Geological Society of America, Boulder, CO.
- Beier, C., Haase, K.M., Abouchami, W., Krienitz, M.-S. & Hauff, F., 2008. Magma genesis by rifting of oceanic lithosphere above anomalous mantle: Terceira Rift, Azores, *Geochem. Geophys. Geosyst.*, **9**, Q12013, doi:10.1029/2008GC002112.
- Bijwaard, H. & Spakman, W., 1999. Tomographic evidence for a narrow whole mantle plume below Iceland, *Earth planet. Sci. Lett.*, **166**(3–4), 121–126.
- Bijwaard, H. & Spakman, W., 2000. Non-linear global P-wave tomography by iterated linearized inversion, *Geophys. J. Int.*, **141**(1), 71–82.
- Bijwaard, H., Spakman, W. & Engdahl, E.R., 1998. Closing the gap between regional and global travel time tomography, *J. geophys. Res.*, **103**(B12), 30 055–30 078.
- Blundell, D.R., Freeman, R., Mueller, S. & S., B., 1992. *A Continent Revealed: The European Geotraverse*, Vol. 4, Cambridge University Press, Cambridge.
- Bock, G. et al., 2001. Seismic probing of Fennoscandian lithosphere, *EOS, Trans. Am. geophys. Un.*, **82**, 621–629.
- de Boorder, H., Spakman, W., White, S. & Wortel, M., 1998. Late cenozoic mineralization, orogenic collapse and slab detachment in the European Alpine belt, *Earth planet. Sci. Lett.*, **164**(3–4), 569–575.
- Boschi, L., Ekström, G. & Kustowski, B., 2004. Multiple resolution surface wave tomography: the Mediterranean Basin, *Geophys. J. Int.*, **157**, 293–304.
- Boschi, L., Fry, B., Ekström, G. & Giardini, D., 2009. The European upper mantle as seen by surface waves, *Surv. Geophys.*, **30**(4–5), 463–501.
- Bozdağ, E., Trampert, J. & Tromp, J., 2011. Misfit functions for full waveform inversion based on instantaneous phase and envelope measurements, *Geophys. J. Int.*, **185**, 845–870.
- Brun, J.-P. & Sokoutis, D., 2010. 45 m.y. of Aegean crust and mantle flow driven by trench retreat, *Geology*, **38**(9), 815–818.

- Bruneton, M. *et al.*, 2004. Complex lithospheric structure under the Central Baltic Shield from surface wave tomography, *J. geophys. Res.*, **109**(B10), doi:10.1029/2003JB002947.
- Cavazza, W., Roure, F., Spakman, W., Stampfli, G. & Ziegler, P., 2004. *The TRANSMED Atlas: The Mediterranean Region from Crust to Mantle*, Vol. 1, Springer, Berlin.
- Chang, S.-J. & van der Lee, S., 2011. Mantle plumes and associated flow beneath Arabia and East Africa, *Earth planet. Sci. Lett.*, **302**(3–4), 448–454.
- Chang, S.-J. *et al.*, 2010. Joint inversion for three-dimensional S-velocity mantle structure along the Tethyan Margin, *J. geophys. Res.*, **115**, doi:10.1029/2009JB007204.
- Cloetingh, S. *et al.*, 2007. Topo-Europe: the geoscience of coupled deep Earth-surface processes, *Glob. planet. Change*, **58**(1–4), 1–118.
- Conrad, C.P., Lithgow-Bertelloni, C. & Loudon, K.E., 2004. Iceland, the Farallon slab, and dynamic topography of the North Atlantic, *Geology*, **32**, 177–180.
- Cotte, N., Pedersen, H. & Group, T.W., 2002. Sharp contrast in lithospheric structure across the Sorgenfrei-Tornquist Zone as inferred by Rayleigh wave analysis of TOR1 project data, *Tectonophysics*, **360**, 75–88.
- Dahlen, F. & Tromp, J., 1998. *Theoretical Global Seismology*, Princeton University Press, Princeton.
- Dalton, C.A., Ekström, G. & Dziewonski, A.M., 2009. Global seismological shear velocity and attenuation: a comparison with experimental observations, *Earth planet. Sci. Lett.*, **284**(1–2), 65–75.
- Dando, B.D.E., Stuart, G.W., Houseman, G.A., Hegedüs, E., Brückel, E. & Radovanović, S., 2011. Teleseismic tomography of the mantle in the Carpathian-Pannonian region of Central Europe, *Geophys. J. Int.*, **186**(1), 11–31.
- Debayle, E., Lévêque, J. & Cara, M., 2001. Seismic evidence for a deeply rooted low-velocity anomaly in the upper mantle beneath the Northeastern Afro/Arabian continent, *Earth planet. Sci. Lett.*, **193**, 423–436.
- Deschamps, F., Trampert, J. & Snieder, R., 2002. Anomalies of temperature and iron in the uppermost mantle inferred from gravity data and tomographic models, *Phys. Earth planet. Inter.*, **129**(3–4), 245–264.
- Doblas, M., 1998. Permo-Carboniferous volcanism in Europe and Northwest Africa: a superplume exhaust valve in the centre of Pangaea? *J. Afr. Earth Sci.*, **26**, 89–99.
- Duggen, S., Hoernle, K.A., Hauff, F., Klugel, A., Bouabdellah, M. & Thirlwall, M.F., 2009. Flow of Canary mantle plume material through a subcontinental lithospheric corridor beneath Africa to the Mediterranean, *Geology*, **37**(3), 283–286.
- Dziewonski, A.M. & Anderson, D.L., 1981. Preliminary reference Earth model, *Phys. Earth planet. Inter.*, **25**, 297–356.
- Dziewonski, A.M., Hager, B.H. & O’Connell, R.J., 1977. Large-scale heterogeneities in the lower mantle, *J. geophys. Res.*, **82**, 239–255.
- Endrun, B., Meier, T., Bischoff, M. & Harjes, H., 2004. Lithospheric structure in the area of Crete constrained by receiver functions and dispersion analysis of Rayleigh phase velocities, *Geophys. J. Int.*, **158**(2), 592–608.
- Endrun, B., Meier, T., Lebedev, S., Bohnhoff, M., Stavrakakis, G. & Harjes, H.-P., 2008. S-velocity structure and radial anisotropy in the Aegean region from surface wave dispersion, *Geophys. J. Int.*, **174**(2), 593–616.
- Endrun, B., Lebedev, S., Meier, T., Tirel, C. & Friederich, W., 2011. Complex layered deformation within the Aegean crust and mantle revealed by seismic anisotropy, *Nature Geosci.*, **4**(2), 203–207.
- Erduran, M., Endrun, B. & T., M., 2008. Continental vs. oceanic lithosphere beneath the Eastern Mediterranean Sea: implications from Rayleigh wave dispersion measurements, *Tectonophysics*, **457**, 42–52.
- Faccenna, C. & Becker, T.W., 2010. Shaping mobile belts by small-scale convection, *Nature*, **465**, 602–605.
- Faccenna, C., Piromallo, C., Crespo-Blanc, A., Jolivet, L. & Rossetti, F., 2004. Lateral slab deformation and the origin of the Western Mediterranean arcs, *Tectonics*, **23**, 1012, doi:10.1029/2002TC001488.
- Faccenna, C., Bellier, O. & Martinod, J., 2006. Slab detachment beneath eastern anatolia: a possible cause for the formation of the North Anatolian Fault, *Earth planet. Sci. Lett.*, **242**(1–2), 85–97.
- Fan, G., Wallace, T. & Zhao, D., 1998. Tomographic imaging of deep velocity structure beneath the eastern and southern Carpathians, Romania: implications for continental collision, *J. geophys. Res.*, **103**, 2705–2723.
- Fichtner, A. & Trampert, J., 2011. Hessian kernels of seismic data functionals based upon adjoint techniques, *Geophys. J. Int.*, **185**, 775–798.
- Fichtner, A., Kennett, B.L.N., Igel, H. & Bunge, H.-P., 2008. Theoretical background for continental- and global-scale full-waveform inversion in the time-frequency domain, *Geophys. J. Int.*, **175**, 665–685.
- Friederich, W. & Meier, T., 2008. Temporary seismic broadband network acquired data on Hellenic Subduction Zone, *EOS, Trans. Am. geophys. Un.*, **89**, 378–378.
- Friederich, W., Wielandt, E. & Stange, S., 1993. Multiple forward scattering of surface waves: comparison with an exact solution and born single-scattering methods, *Geophys. J. Int.*, **112**, 264–275.
- Friederich, W., Wielandt, E. & Stange, S., 1994. Non-plane geometries of seismic surface wavefields and their implications for regional surface-wave tomography, *Geophys. J. Int.*, **119**, 931–948.
- Fry, B., Boschi, L., Ekström, G. & Giardini, G., 2008. Europe-Mediterranean tomography: high correlation between new seismic data and independent geophysical observables, *Geophys. Res. Lett.*, **35**(4), L04301.1–L04301.5.
- Gee, D. & Stephenson, R., 2006. *European Lithosphere Dynamics*, Geological Society, London.
- Geissler, W.H., Sodoudi, F. & Kind, R., 2010. Thickness of the Central and Eastern European lithosphere as seen by S receiver functions, *Geophys. J. Int.*, **181**, 604–634.
- Gossler, J., Kind, R., Sobolev, S., Kampf, H., Wylegalla, K., Stiller, M. & Grp, T.W., 1999. Major crustal features between the Harz Mountains and the Baltic Shield derived from receiver functions, *Tectonophysics*, **314**(1–3), 321–333.
- Grand, S., van der Hilst, R. & Widiyantoro, S., 1997. Global seismic tomography: a snapshot of convection in the Earth, *GSA Today*, **7**, 1–7.
- Grand, S.P., 2002. Mantle shear-wave tomography and the fate of subducted slabs, *Phil. Trans. R. Soc. Lond., A*, **360**, 2475–2491.
- Granet, M., 1986. A teleseismic study of the upper Rhine Graben area: array mislocation diagram and 3-D inversion, *J. geophys. Res.*, **59**, 119–128.
- Granet, M., Wilson, M. & Achauer, U., 1995. Imaging a mantle plume beneath the French Massif Central, *Earth planet. Sci. Lett.*, **136**, 281–296.
- Gregersen, S., Voss, P., Nielsen, L., Achauer, U., Busche, H., Rabbal, W. & Shomali, Z., 2010. Uniqueness of modeling results from teleseismic P-wave tomography in Project Tor, *Tectonophysics*, **481**, 99–107.
- Handy, M.R., Schmid, S.M., Bousquet, R., Kissling, E. & Bernoulli, D., 2010. Reconciling plate-tectonic reconstructions of Alpine Tethys with the geological-geophysical record of spreading and subduction in the Alps, *Earth Sci. Rev.*, **102**, 121–158.
- Harangi, S., Downes, H. & Seghedi, I., 2006. Tertiary-quaternary subduction processes and related magmatism in the Alpine-Mediterranean region, *Geol. Soc. Lond. Mem.*, **32**, 167–190, doi:10.1144/GSL.MEM.2006.032.01.10.
- Heeremans, M., Faleide, J.I. & Larsen, B.T., 2004. Late Carboniferous-Permian of NW Europe: an introduction to a new regional map, *Geol. Soc. Lond. Spec. Publ.*, **223**(1), 75–88.
- Helmberger, D., Wen, L. & Ding, X., 1998. Seismic evidence that the source of the Iceland Hotspot lies at the core-mantle boundary, *Nature*, **396**(6708), 251–255.
- van Hinsbergen, D.J.J., Hafkenscheid, E., Spakman, W., Meulenkamp, J.E. & Wortel, R., 2005. Nappe stacking resulting from subduction of oceanic and continental Lithosphere below Greece, *Geology*, **33**, 325–328.
- Hoernle, K., Zhang, Y.-S. & Graham, D., 1995. Seismic and geochemical evidence for large-scale mantle upwelling beneath the Eastern Atlantic and Western and Central Europe, *Nature*, **374**, 34–39.
- Jans, A.B. & Sheahan, P.A., 1995. Catalogue of world wide diamond and kimberlite occurrences: a selective and annotative approach, *J. Geochem. Explor.*, **53**(1–3), 73–111.
- Jolivet, L., Faccenna, C. & Piromallo, C., 2009. From mantle to crust: stretching the Mediterranean, *Earth planet. Sci. Lett.*, **285**(1–2), 198–209.
- Judenherc, S., Granet, M. & Boumbar, N., 1999. Two-dimensional anisotropic tomography of lithosphere beneath France using regional arrival times, *J. geophys. Res.*, **104**, 13 201–13 215.
- Kaiser, A., Reicherter, K., Hübscher, C. & Gajewski, D., 2005. Variation of the present-day stress field within the North German Basin-insights from

- thin shell FE modeling based on residual GPS velocities, *Tectonophysics*, **397**, 55–72.
- Karason, H. & van der Hilst, R., 2000. Constraints on mantle convection from seismic tomography, *Geophys. Monogr.*, **121**, 277–288.
- Kassaras, I., Makropoulos, K., Bourouva, E., Pedersen, H. & Hatzfeld, D., 2005. Upper mantle structure of the Aegean derived from two-station phase velocities of fundamental mode Rayleigh waves, in *Developments in Volcanology*, Vol. 7, Elsevier, Berlin.
- Kennett, B.L.N., Engdahl, E.R. & Buland, R., 1995. Constraints on seismic velocities in the Earth from traveltimes, *Geophys. J. Int.*, **122**, 108–124.
- Keyser, M., Ritter, J. & Jordan, M., 2002. 3D shear-wave velocity structure of the Eiffel Plume, Germany, *Earth planet. Sci. Lett.*, **203**, 59–82.
- Khan, A., Boschi, L. & Connolly, J.A.D., 2011. Mapping the Earth's thermochemical and anisotropic structure using global surface wave data, *J. geophys. Res.*, **116**, 1301.
- Kissling, E. & Spakman, W., 1996. Interpretation of tomographic images of uppermost mantle structure: examples from the Western and Central Alps, *J. Geodyn.*, **21**(1), 97–111.
- Kissling, E., Schmid, S.M., Lippitsch, R., Ansorge, J. & Fügenschuh, B., 2006. Lithosphere structure and tectonic evolution of the Alpine Arc: new evidence from high-resolution teleseismic tomography, *Geol. Soc. Lond. Mem.*, **32**(1), 129–145.
- Korja, T., 2007. How is the European lithosphere imaged by magnetotellurics? *Surv. Geophys.*, **28**, 239–272.
- Koulakov, I., Tychkov, S., Bushenkova, N. & Vasilevsky, A., 2002. Structure and dynamics of the upper mantle beneath the Alpine-Himalayan orogenic belt, from teleseismic tomography, *Tectonophysics*, **358**(1–4), 77–96.
- Koulakov, I., Kaban, M., Tesauro, M. & Cloetingh, S., 2009. P- and S-velocity anomalies in the upper mantle beneath Europe from tomographic inversion of ISC data, *Geophys. J. Int.*, **179**, 345–366.
- Kustowski, B., Ekström, G. & Dziewonski, A.M., 2008. The shear-wave velocity structure in the upper mantle beneath Eurasia, *Geophys. J. Int.*, **174**(3), 978–992.
- Lebedev, S. & van der Hilst, R.D., 2008. Global upper-mantle tomography with the automated multimode inversion of surface and S-wave forms, *Geophys. J. Int.*, **173**(2), 505–518.
- Lebedev, S., Nolet, G. & van der Hilst, R.D., 1997. The upper mantle beneath the Philippine Sea region from waveform inversions, *Geophys. Res. Lett.*, **24**, 1851–1854.
- Lebedev, S., Nolet, G., Meier, T. & van der Hilst, R., 2005. Automated multimode inversion of surface and S-waveforms, *Geophys. J. Int.*, **162**, 951–964.
- Lebedev, S., Meier, T. & van der Hilst, R., 2006. Asthenospheric flow and origin of volcanism in the Baikal Rift area, *Earth planet. Sci. Lett.*, **249**(3–4), 415–424.
- Lekić, V. & Romanowicz, B., 2011a. Inferring upper-mantle structure by full waveform tomography with the Spectral Element Method, *Geophys. J. Int.*, **185**, 799–831.
- Lekić, V. & Romanowicz, B., 2011b. Tectonic regionalization without a priori information: a cluster analysis of upper mantle tomography, *Earth planet. Sci. Lett.*, **308**, 151–160.
- Levshin, A.L., Barmin, M.P., Ritzwoller, M.H. & Trampert, J., 2005. Minor-arc and major-arc global surface wave diffraction tomography, *Phys. Earth planet. Inter.*, **149**, 205–223.
- Levshin, A., Schweitzer, J., Weidle, C., Shapiro, N. & Ritzwoller, M., 2007. Surface wave tomography of the Barents Sea and surrounding regions, *Geophys. J. Int.*, **170**, 441–459.
- Li, A. & Detrick, R., 2003. Azimuthal anisotropy and phase velocity beneath Iceland: implication for plume-ridge interaction, *Earth planet. Sci. Lett.*, **214**(1–2), 153–165.
- Lin, F.-C., Ritzwoller, M.H. & Snieder, R., 2009. Eikonal tomography: surface wave tomography by phase front tracking across a regional broadband seismic array, *Geophys. J. Int.*, **177**(3), 1091–1110.
- Lippitsch, R., Kissling, E. & Ansorge, J., 2003. Upper mantle structure beneath the Alpine orogen from high-resolution teleseismic tomography, *J. geophys. Res.*, **108**, 2376–2391.
- Lonsdale, P. & Shor, A., 1979. The oblique intersection of the Mid-Atlantic Ridge with Charlie-Gibbs transform fault, *Tectonophysics*, **54**, 195–209.
- Lustrino, M. & Wilson, M., 2007. The circum-Mediterranean anorogenic Cenozoic igneous province, *Earth Sci. Rev.*, **81**, 1–65.
- Marone, F., van der Lee, S. & Giardini, D., 2004a. Three-dimensional upper-mantle S-velocity model for the Eurasia-Africa plate boundary region, *Geophys. J. Int.*, **158**(1), 109–130.
- Marone, F., van der Lee, S. & Giardini, D., 2004b. Shallow anisotropy in the Mediterranean mantle from surface waves, *Geophys. Res. Lett.*, **31**(6), doi:10.1029/2003GL018948.
- Marquering, H., Snieder, R. & Nolet, G., 1996. Waveform inversions and the significance of surface-wave mode coupling, *Geophys. J. Int.*, **124**(1), 258–278.
- Masters, G., Laske, G., Bolton, H. & Dziewonski, A., 2000. The relative behavior of shear velocity, bulk sound speed, and compressional velocity in the mantle: implications for chemical and thermal structure, *Geophys. Monogr. Ser.*, **117**, 63–87, doi:10.1029/GM117p0063.
- Mathar, J.P., Ritter, J.R.R. & Friederich, W., 2006. Fast Track Paper: Surface waves image the top of the Eifel plume, *Geophys. J. Int.*, **164**, 377–382.
- van der Meer, D.G., Spakman, W., van Hinsbergen, D.J.J., Amaru, M.L. & Torsvik, T.H., 2010. Towards absolute plate motions constrained by lower-mantle slab remnants, *Nature Geosci.*, **3**(1), 36–40.
- Mégnin, C. & Romanowicz, B., 2000. The three-dimensional shear velocity structure of the Mantle from the inversion of body, surface and higher-mode waveforms, *Geophys. J. Int.*, **143**, 709–728.
- Meier, T., Malischewsky, P. & Neunhofer, H., 1997a. Reflection and transmission of surface waves at a vertical discontinuity and imaging of lateral heterogeneity using reflected fundamental Rayleigh waves, *Bull. seism. Soc. Am.*, **87**(6), 1648–1661.
- Meier, T., Lebedev, S., Nolet, G. & Dahlen, F.A., 1997b. Diffraction tomography using multimode surface waves, *J. geophys. Res.*, **102**, 8255–8268.
- Meier, T., Dietrich, K., Stöckhert, B. & Harjes, H., 2004. One-dimensional models of shear wave velocity for the Eastern Mediterranean obtained from the inversion of rayleigh wave phase velocities and tectonic implications, *Geophys. J. Int.*, **156**, 45–58.
- Meier, T., Becker, D., Endrun, B., Rische, M., Bohnhoff, M., Stöckhert, B. & Harjes, H.-P., 2007. A model for the Hellenic Subduction Zone in the area of Crete based on seismological investigations, *Geol. Soc. Lond. Spec. Publ.*, **291**(1), 183–199.
- Mocquet, A., Romanowicz, B. & Montagner, J.P., 1989. Three-dimensional structure of the upper mantle beneath the Atlantic Ocean inferred from long-period Rayleigh waves I. Group and phase velocity distributions, *J. geophys. Res.*, **94**, 7449–7468.
- Montelli, R., Nolet, G., Dahlen, F.A. & Masters, G., 2006. A catalogue of deep mantle plumes: new results from finite-frequency tomography, *Geochem. Geophys. Geosyst.*, **7**, Q11007–Q11076.
- Nolet, G., 1990. Partitioned waveform inversion and two-dimensional structure under the network of autonomously recording seismographs, *J. geophys. Res.*, **95**(B6), 8499–8512.
- Nolet, G. & Zielhuis, A., 1994. Low S-velocities under the Tornquist-Teisseyre zone: evidence for water injection into the transition zone by subduction, *J. geophys. Res.*, **99**(B8), 15 813–15 820.
- Nolet, G., Grand, S.P. & Kennett, B.L.N., 1994. Seismic heterogeneity in the upper-mantle, *J. geophys. Res.*, **99**(B12), 23 753–23 766.
- O'Donnell, J.P., Daly, E., Tiberi, C., Bastow, I.D., O'Reilly, B.M., Readman, P.W. & Hauser, F., 2011. Lithosphere-Asthenosphere interaction beneath Ireland from joint inversion of teleseismic P-wave delay times and GRACE gravity, *Geophys. J. Int.*, **184**, 1379–1396.
- Paige, C. & Saunders, M., 1982. LSQR: an algorithm for sparse linear equations and sparse least squares, *Trans. Math. Softw.*, **8**(1), 43–71.
- Panning, M. & Romanowicz, B., 2006. A three-dimensional radially anisotropic model of shear velocity in the whole Mantle, *Geophys. J. Int.*, **167**(1), 361–379.
- Panza, G., Raykova, R., Carminati, E. & Doglioni, C., 2007. Upper mantle flow in the Western Mediterranean, *Earth planet. Sci. Lett.*, **257**, 200–214.
- Pasyanos, M.E. & Nyblade, A.A., 2007. A top to bottom lithospheric study of Africa and Arabia, *Tectonophysics*, **444**(1–4), 27–44.
- Peter, D., Tape, C., Boschi, L. & Woodhouse, J.H., 2007. Surface wave tomography: global membrane waves and adjoint methods, *Geophys. J. Int.*, **171**, 1098–1117.

- Peter, D., Boschi, L., Deschamps, F., Fry, B., Ekström, G. & Giardini, D., 2008. A new finite-frequency shear-velocity model of the European-Mediterranean region, *Geophys. Res. Lett.*, **35**(16), doi:10.1029/2008GL034769.
- Pilidou, S., Priestley, K., Debayle, E. & Gudmundsson, O., 2005. Rayleigh wave tomography in the North Atlantic: high resolution images of the Iceland, Azores and Eifel mantle plumes, *Lithos*, **79**(3–4), 453–474.
- Piomallo, C. & Morelli, A., 1997. Imaging the Mediterranean upper mantle by P- wave travel time tomography, *Ann. Geofis.*, **XL**(4), 963–979.
- Piomallo, C. & Morelli, A., 2003. P wave tomography of the mantle under the Alpine-Mediterranean area, *J. geophys. Res.*, **108**(B2), doi:10.1029/2002JB001757.
- Piomallo, C., Vincent, A.P., Yuen, D.A. & Morelli, A., 2001. Dynamics of the transition zone under Europe inferred from wavelet cross-spectra of seismic tomography, *Phys. Earth planet. Inter.*, **125**(1–4), 125–139.
- Plomerová, J. & Babuška, V., 2010. Long memory of mantle lithosphere fabric—European LAB constrained from seismic anisotropy, *Lithos*, **120**, 131–143.
- Plomerová, J., Babuška, V., Vecsey, L., Kouba, D. & Group, T.W., 2002. Seismic anisotropy of the lithosphere around the Trans-European Suture Zone (TESZ) based on teleseismic body-wave data of the TOR experiment, *Tectonophysics*, **360**, 89–114.
- Plomerová, J., Achauer, U., Babuška, V. & Vecsey, L., 2007. Upper mantle beneath the Eger Rift (central Europe): plume or asthenosphere upwelling? *Geophys. J. Int.*, **169**, 675–682.
- Polat, G., Lebedev, S., Readman, P.W., O'Reilly, B.M. & Hauser, F., 2012. Anisotropic Rayleigh-wave tomography of Ireland's crust: implications for crustal accretion and evolution within the Caledonian Orogen, *Geophys. Res. Lett.*, **39**, L04302, doi:10.1029/2012GL051014.
- Priestley, K. & McKenzie, D., 2006. The thermal structure of the lithosphere from shear wave velocities, *Earth planet. Sci. Lett.*, **244**, 285–301.
- Qin, Y., Capdeville, Y., Maupin, V., Montagner, J.-P., Lebedev, S. & Beucler, E., 2008. SPICE benchmark for global tomographic methods, *Geophys. J. Int.*, **175**, 598–616.
- Rawlinson, A., Pozgay, S. & Fishwick, S., 2010. Seismic tomography: a window into deep Earth, *Phys. Earth planet. Inter.*, **178**(3–4), 101–135.
- Raykova, R. & Panza, G., 2006. Surface waves tomography and non-linear inversion in the Southeast Carpathians, *Phys. Earth planet. Inter.*, **157**(3–4), 164–180.
- Ritsema, J., van Heijst, H. & Woodhouse, J., 1999. Complex shear wave velocity structure imaged beneath Africa and Iceland, *Science*, **286**(5446), 1925–1928.
- Ritsema, J., van Heijst, H.J. & Woodhouse, J.H., 2004. Global transition zone tomography, *J. geophys. Res.*, **109**, B02302, doi:10.1029/2003JB002610.
- Ritsema, J., Deuss, A., van Heijst, H. & Woodhouse, J., 2011. S4ORTS: a degree-40 shear-velocity model for the mantle from new rayleigh wave dispersion, teleseismic traveltime and normal-mode splitting function measurements, *Geophys. J. Int.*, **184**(3), 1223–1236.
- Ritter, J.R.R., Jordan, M. & Christensen, U., 2001. A mantle plume below the Eifel volcanic fields, Germany, *Earth planet. Sci. Lett.*, **186**(1), 7–14.
- Ritzwoller, M. & Levshin, A., 1998. Eurasian surface wave tomography: group velocities, *J. geophys. Res.*, **103**, 4839–4878.
- Ritzwoller, M.H., Shapiro, N.M., Barmin, M.P. & Levshin, A.L., 2002. Global surface wave diffraction tomography, *J. geophys. Res.*, **107**(B12), 2335, doi:10.1029/2002JB001777.
- Rohrman, M. & van der Beek, P., 1996. Cenozoic postrift domal uplift of North Atlantic margins: an asthenospheric diapirism model, *Geology*, **24**, 901–904.
- Romanowicz, B., 2003. 3D structure of the Earth's lower mantle, *C. R. Geosci.*, **335**(1), 23–35.
- Schäfer, J.F., Boschi, L. & Kissling, E., 2011. Adaptively parametrized surface wave tomography: methodology and a new model of the European Upper Mantle, *Geophys. J. Int.*, **186**(3), 1431–1453.
- Scheck, M., Bayer, U., Otto, V., Lamarche, J., Banka, D. & Pharaoh, T., 2002. The Elbe fault system in north central Europe—a basement controlled zone of crustal weakness, *Tectonophysics*, **360**(1–4), 281–299.
- Schivardi, R. & Morelli, A., 2009. Surface wave tomography in the European and Mediterranean region, *Geophys. J. Int.*, **177**(3), 1050–1066.
- Schmid, C., van der Lee, S., VanDecar, J.C., Engdahl, E.R. & Giardini, D., 2008. Three-dimensional S-velocity of the mantle in the Africa-Eurasia plate boundary region from phase arrival times and regional waveforms, *J. geophys. Res.*, **113**(B3), doi:10.1029/2005JB004193.
- Schweitzer, J., 2005. Blockage of regional seismic waves by the Teisseyre-Tornquist Zone, *Geophys. J. Int.*, **123**(1), 260–276.
- Sebai, A., Stutzmann, E., Montagner, J.-P., Sicilia, D. & Beucler, E., 2006. Anisotropic structure of the African upper mantle from Rayleigh and Love wave tomography, *Phys. Earth planet. Inter.*, **155**(1–2), 48–62.
- Shapiro, N., Campillo, M., Stehly, L. & Ritzwoller, M., 2005. High-resolution surface-wave tomography from ambient seismic noise, *Science*, **307**(5715), 1615–1618.
- Shen, Y., Solomon, S. & Bjarnason, I., 1996. Hot Mantle Transition Zone beneath Iceland and the adjacent Mid-Atlantic ridge inferred from p-to-s conversions at the 410- and 660-km, *Geophys. Res. Lett.*, **23**(24), 3527–3530.
- Shen, Y., Solomon, S. & Bjarnason, I., 2002. Seismic evidence for a tilted mantle plume and north-south mantle flow beneath Iceland, *Earth planet. Sci. Lett.*, **197**(3–4), 261–272.
- Shomali, Z.H., Roberts, R.G. & TOR Working Group., 2002. Non-linear body wave teleseismic tomography along the TOR array, *Geophys. J. Int.*, **148**(3), 562–574.
- Shomali, Z.H., Roberts, R.G. & Pedersen, L.B., 2006. Lithospheric structure of the Tornquist Zone resolved by nonlinear P- and S-teleseismic tomography along the TOR array, *Tectonophysics*, **416**(1–4), 133–149.
- Silveira, G. & Stutzmann, E., 2002. Anisotropic tomography of the Atlantic Ocean, *Phys. Earth planet. Inter.*, **132**, 237–248.
- Simmons, N.A., Forte, A.M., Boschi, L. & Grand, S.P., 2010. GyPSuM: a joint tomographic model of mantle density and seismic wave speeds, *J. geophys. Res.*, **115**, B12310, doi:10.1029/2010JB007631.
- Sobolev, S., 1997. Upper mantle temperatures and lithosphere-asthenosphere system beneath the French Massif Central constrained by seismic, gravity, petrologic and thermal observations, *Tectonophysics*, **275**, 143–164.
- Souriau, A., Chevrot, S. & Olivera, C., 2008. A new tomographic image of the Pyrenean lithosphere from teleseismic data, *Tectonophysics*, **460**, 206–214.
- Spakman, W., 1988. Upper mantle delay time tomography: with an application to the collision zone of the Eurasian, African and Arabian plates, *PhD thesis*, Utrecht University.
- Spakman, W. & Wortel, M., 2004. *The TRANSMED Atlas: Tomographic View on Western Mediterranean Geodynamics*, Vol. 1, Springer, Berlin.
- Spakman, W., Vanderlee, S. & Vanderhilst, R., 1993. Travel-time tomography of the European Mediterranean mantle down to 1400 km, *Phys. Earth planet. Inter.*, **79**(1–2), 3–74.
- Thompson, R. & Gibson, S., 1991. Subcontinental mantle plumes, hotspots and pre-existing thinspots, *J. geol. Soc. Lond.*, **148**(Part 6), 973–977.
- Timmerman, M.J., Heeremans, M., Kirstein, L.A., Tore Larsen, B., Spence-Dunworth, E.-A. & Sundvoll, B., 2009. Linking changes in tectonic style with magmatism in Northern Europe during the late Carboniferous to latest Permian, *Tectonophysics*, **473**, 375–390.
- Trampert, J. & Woodhouse, J.H., 1995. Global phase velocity maps of Love and Rayleigh waves between 40 and 150 seconds, *Geophys. J. Int.*, **122**(2), 675–690.
- Trampert, J. & Woodhouse, J.H., 1996. High resolution global phase velocity distributions, *Geophys. Res. Lett.*, **23**, 21–24.
- Vaccari, F. & Panza, G., 1993. Vp/Vs estimation in Southwestern Europe from P-wave and surface-wave tomography analysis, *Phys. Earth planet. Inter.*, **78**, 229–237.
- Villaseñor, A., Ritzwoller, M. & Levshin, A., 2001a. Shear velocity structure of Central Eurasia from inversion of surface wave velocities, *Phys. Earth planet. Inter.*, **123**(2–4), 169–184.
- Villaseñor, A., Ritzwoller, M., Levshin, A., Barmin, M., Engdahl, E., Spakman, W. & Trampert, J., 2001b. Shear velocity structure of Central Eurasia from inversion of surface wave velocities, *Phys. Earth planet. Inter.*, **123**, 169–184.

- Wawerzinek, B., Ritter, J.R.R., Jordan, M. & Landes, M., 2008. An upper-mantle upwelling underneath Ireland revealed from non-linear tomography, *Geophys. J. Int.*, **175**, 253–268.
- Wedepohl, K.H. & Baumann, A., 1999. Central European Cenozoic plume volcanism with OIB characteristics and indications of a lower mantle source, *Computer*, **136**, 225–239.
- Weidle, C. & Maupin, V., 2008. An upper-mantle S-wave velocity model for Northern Europe from Love and Rayleigh group velocities, *Geophys. J. Int.*, **175**(3), 1154–1168.
- Wessel, P. & Smith, W.H.F., 1995. New version of the Generic Mapping Tools Released, *EOS Trans. Am. geophys. Un.*, **76**, 329.
- White, N. & Lovell, B., 1997. Measuring the pulse of a plume with the sedimentary record, *Nature*, **387**, 888–891.
- White, R.S., 1988. A hot-spot model for early tertiary volcanism in the North Atlantic, *Geol. Soc. Lond. Spec. Publ.*, **39**(1), 3–13.
- Wielandt, E., 1993. Propagation and structural interpretation of non-plane waves, *Geophys. J. Int.*, **113**, 45–53.
- Wilson, M. & Downes, H., 1991. Tertiary-quadernary extension-related alkaline magmatism in Western and Central Europe, *J. Petrol.*, **32**(4), 811–849.
- Woodhouse, J., 1974. Surface waves in a laterally varying layered structure, *Geophys. J. R. astr. Soc.*, **37**(3), 461–490.
- Woodhouse, J.H. & Dziewonski, A.M., 1984. Mapping the upper mantle: three dimensional modeling of Earth structure by inversion of seismic waveforms, *J. geophys. Res.*, **89**, 5953–5986.
- Wortel, M. & Spakman, W., 2000. Subduction and slab detachment in the Mediterranean-Carpathian Region, *Science*, **290**(5498), 1910–1917.
- Zhang, Y.-S. & Tanimoto, T., 1993. High-resolution global upper mantle structure and plate tectonics, *J. geophys. Res.*, **98**, 9793–9823.
- Zhou, Y., Nolet, G., Dahlen, F.A. & Laske, G., 2006. Global upper-mantle structure from finite-frequency surface-wave tomography, *J. geophys. Res.*, **111**, B04304, doi:10.1029/2005JB003677.
- Ziegler, P., 1986. Geodynamic model for the Palaeozoic crustal consolidation of Western and Central Europe, *Tectonophysics*, **126**, 303–328.
- Zielhuis, A. & Nolet, G., 1994. Shear-wave velocity variations in the upper-mantle beneath Central Europe, *Geophys. J. Int.*, **117**(3), 695–715.